Version dated: January 23, 2023

Deep learning approaches to viral phylogeography are fast and as robust as likelihood methods to model misspecification

Ammon Thompson[1,*], Benjamin Liebeskind[1], Erik J. Scully[1], Michael Landis[2,*]

[1]*National Geospatial-Intelligence Agency, Springfield, VA, 22150, USA*

[2]*Department of Biology, Washington University in St. Louis, Rebstock Hall, St. Louis, Missouri, 63130, USA*

[*]**Corresponding authors:** E-mail: Ammon.M.Thompson.ctr@nga.mil and michael.landis@wustl.edu.

Abstract.— Analysis of phylogenetic trees has become an essential tool in epidemiology. Likelihood-based methods fit models to phylogenies to draw inferences about the phylodynamics and history of viral transmission. However, these methods are computationally expensive, which limits the complexity and realism of phylodynamic models and makes them ill-suited for informing policy decisions in real-time during rapidly developing outbreaks. Likelihood-free methods using deep learning are pushing the boundaries of inference beyond these constraints. In this paper, we extend, compare and contrast a recently developed deep learning method for likelihood-free inference from trees. We trained multiple deep neural networks using phylogenies from simulated outbreaks that spread among five locations and found they achieve similar levels of accuracy to Bayesian inference under the true simulation model. We compared robustness to model misspecification of a trained neural network to that of a Bayesian method. We found that both models had comparable performance, converging on similar biases. We also trained and tested a neural network against phylogeographic data from a recent study of the SARS-Cov-2 pandemic in Europe and obtained similar estimates of epidemiological parameters and the location of the common ancestor in Europe. Along with being as accurate and robust as likelihood-based methods, our trained neural networks are on average over 3 orders of magnitude faster. Our results support the notion that neural networks can be trained with simulated data to accurately mimic the good and bad statistical properties of the likelihood functions of generative phylogenetic models.

(Keywords: phylogeography, SSE, phylodynamics, machine learning, deep learning, epidemiology)

Introduction

Viral phylodynamic models use genomes sampled from infected individuals to trace the evolutionary history of a pathogen and its spread through a population (Holmes and Garnett 1994; Volz et al. 2013). By linking genetic information to epidemiological data, such as the location and time of sampling, these generative models can provide valuable insights into the transmission dynamics of infectious diseases, especially in the early stages of cryptic disease spread when it is more difficult to detect and track (Holmes et al. 1995; Rambaut et al. 2008; Lemey et al. 2009; Pybus et al. 2012; Worobey et al. 2016, 2020; Lemey et al. 2021; Washington et al. 2021; Pekar et al. 2022). This information can be used to inform public health interventions and improve our understanding of the evolution and spread of pathogens. Many phylodynamic models are adapted from state-dependent birth-death (SDBD) processes or, equivalently, state-dependent speciation-extinction (SSE) models (Maddison et al. 2007; FitzJohn 2012; Kühnert et al. 2014; Beaulieu and O'Meara 2016). Here, we will refer to the state as location and the models as location-dependent birth-death (LDBDS) models which include serial sampling (Kühnert et al. 2016).

Epidemiologists are increasingly using LDBDS models to estimate transmission rates, migration rates between locations, and variation in these rates amongst populations (Nadeau et al. 2021) and species (Lu et al. 2021). Analysts fit data to these models with likelihood-based inference methods, such as maximum likelihood (Maddison et al. 2007; Richter et al. 2020) or Bayesian Markov chain Monte Carlo (Kühnert et al. 2016; Scire et al. 2020). Likelihood-based inference relies upon a likelihood function to evaluate the relative probability (likelihood) that a given phylogenetic pattern (i.e., topology, branch lengths, and tip locations) was generated by a phylodynamic process with particular model parameter values. In this sense the likelihood of any possible phylodynamic data set is mathematically encoded into the likelihood as a function of (unknown) data-generating model parameters.

Computing the likelihood requires high-dimensional integration over a large and

complex space of evolutionary histories. Analytically integrated likelihood functions, however, are not known for LDBDS models. Methods developers instead use ordinary differential equation (ODE) solvers (Maddison et al. 2007; Kühnert et al. 2016) or data augmentation (DA) methods (Maliet et al. 2019) to numerically approximate the integrated likelihood. These clever approximations perform well statistically, but are too computationally expensive to use with large epidemic-scale data sets. Thus, while Nextstrain (Hadfield et al. 2018) and similar efforts provided useful visualizations to policy makers during the COVID response, most phylogeographical methods are used forensically, providing insight on the past, and are not used to provide parameter estimates in response to emerging events to inform policy decisions in real-time due to the complexity and long run-times of these models.

As phylodynamic models become more biologically realistic, they will necessarily grow more mathematically complex, and therefore less able to yield likelihood functions that can be approximated using ODE or DA methods. Because of this, phylodynamic model developers tend to explore only models for which a likelihood-based inference strategy is readily available. As a consequence, this impedes the design, study, and application of richer phylodynamic models of disease transmission.

To avoid the computational limitations associated with likelihood-based methods, deep learning inference methods that are likelihood-free have emerged as a complementary framework for fitting a wide variety of evolutionary models (Bokma 2006). Deep learning methods rely on training many-layered neural networks to extract information from data patterns. These neural networks can be trained with simulated data as another way to approximate the latent likelihood function (Cranmer et al. 2020). Once trained, neural networks have the benefit of being fast, easy to use, and scalable. Recently, likelihood-free deep learning neural network methods have successfully been applied to phylogenetics (Suvorov et al. 2020; Suvorov and Schrider 2022b; Nesterenko et al. 2022; Solis-Lemus et al. 2022; da Fonseca et al. 2020), and phylodynamic inference (Voznica et al. 2022;

Lambert et al. 2022).

Here we extend new methods of deep learning from phylogenetic trees (Voznica et al. 2021; Lambert et al. 2022) to explore their potential when applied to phylogeographic problems in geospatial epidemiology. Phylodynamics of birth-death-sampling processes that include migration among locations have been under development for more than a decade (Stadler 2010; Stadler et al. 2012; Kühnert et al. 2014, 2016; Scire et al. 2020; Gao et al. 2021, 2022). Given the added complexity of location specific dynamics (e.g. location specific birth rates) and recent successes in deep learning with phylogenetic time trees (Voznica et al. 2022) under state-dependent diversification models (Lambert et al. 2022), we sought to evaluate this approach when applied to viral phylodynamics and phylogeography by including location data when training deep neural networks with phylogenetic trees.

One important limitation of likelihood-free approaches is that it is unknown how brittle the inference machinery is when the assumptions used for simulation and training are violated (Schmitt et al. 2022). For example, a brittle deep learning method would be more easily mislead by model misspecification when compared to a likelihood-based method. Likelihood approaches may have some advantages because the simplifying assumptions are explicit in the likelihood function while for trained neural networks it is difficult to know how those assumptions are encoded for any given implementation. However, with complex likelihood models, there may be unexpected interactions among simplifying assumptions that result in large biases when applied to real-world data. Characterizing the relative robustness and brittleness of these two inference paradigms is essential for those who wish to confidently develop and deploy likelihood-free methods of inference from real world data.

To explore relative robustness to model misspecification, we trained multiple deep convolutional neural networks (CNNs) with transmission trees generated from epidemic simulations. We show that simulation-trained CNNs are not only as accurate as likelihood-based approaches but are no more sensitive to model violations than the

likelihood approach. Both methods consistently show similar biases induced by model violations in test data sets. We find that for the models tested here, the migration rate estimates are highly sensitive to misspecification of infection rate and sampling rates, but that estimates of the infection and sampling rates are fairly robust to misspecification of the migration models. We also show that the rate parameter estimates are fairly robust to misspecification of both the number of locations in the model and phylogenetic error. Finally, we compared a simulation-trained neural network to a recent phylodynamic study of the first wave of the COVID pandemic in Europe (Nadeau et al. 2021) and obtain similar inferences about the dynamics and history of SARS-CoV-2 in the European clade.

Methods

LDBDS processes are stochastic branching processes that define location-dependent rates for birth, death, migration, and sampling events to randomly generate time-scaled phylogenies where taxa are associated with various locations. With serial sampling, many chains of the transmission tree go undetected. Consequently, in phylogeography an absence of evidence is not evidence of absence in time and space. This fact requires simulation of not just the sampled/observed phylogenetic tree but the evolution of the underlying population from which it is sampled. This underlying population is divided into compartments of Susceptible individuals, infectious individuals, and recovered/non-susceptable individuals. The dynamics of these compartments are describe by the Susceptible-Infectious-Recovered (SIR) compartmental model.

First, we define the SIR model we assume here that is approximately equivalent to the LDBDS model (Kühnert et al. 2016). Following that, is a description of the simulation method to generate the training, validation, and test data sets of phylogenies under the model. We next describe our implementation of simulation-trained deep learning inference with convolutional neural networks (CNN) as well as a likelihood-based method using Bayesian inference. We then describe our methods for measuring and comparing their

performance when tested against data sets generated by simulations under the inference model as well as several data sets simulated under models that violate assumptions of the inference model. Finally, we describe how we tested our simulation-trained CNN against a real-world data set.

Model definition

We first define a general location-dependent SIR stochastic process used for simulations and likelihood function derivation in the format of reaction equations we specified in MASTER (Vaughan and Drummond 2013). Reaction equations 1 through 4 specify the SIR compartment model with migration and serial sampling where S, I, and R denote the number of individuals in each compartment. The S and I compartments are indexed by geographic location using i and j. N_i is the total population size in location i and $N_i = S_i + I_i + R_i$. The symbols for each rate parameter is placed above each reaction arrow.

$$S_i + I_i \xrightarrow{\beta_i/N_i} 2I_i \qquad \text{infection} \tag{1}$$

$$I_i \xrightarrow{m_{ij}} I_j \qquad \text{migration} \tag{2}$$

$$I_i \xrightarrow{\gamma} R \qquad \text{recovery} \tag{3}$$

$$I_i \xrightarrow{\delta_i} R \qquad \text{sample and recovery.} \tag{4}$$

We parameterize the model with the basic reproduction number in location i, R_{0_i}, which is related to β_i and δ_i by equation 5,

$$R_{0_i} = \frac{\beta_i}{\gamma + \delta_i}. \tag{5}$$

In particular, our study considers a location-independent SIR (LI-SIR) model with sampling that assumes R_{0_i} was equal among all locations, and a location-dependent

(LD-SIR) model with sampling that assumes R_{0_i} varied among locations. During the exponential growth phase of an outbreak, the LI-SIR and LD-SIR models are equivalent to the location-independent birth-death-sampling (LIBDS) and location-dependent birth-death-sampling (LDBDS) models, respectively, that are often used in viral phylogeography (Kühnert et al. 2014, 2016; Douglas et al. 2021).

Each infectious individual transitions to recovered at rate γ. We assumed that sampling a virus in an individual occurs at rate δ_i in location i and immediately removes that individual from the infectious compartment and places them in the recovered compartment. Thus the effective recovery rate in location i is $\gamma + \delta_i$. The above reactions correspond to the following coupled ordinary differential equations.

$$\begin{aligned}
\frac{dS_i}{dt} &= -\frac{\beta_i}{N_i} S_i I_i \\
\frac{dI_i}{dt} &= \frac{\beta_i}{N_i} S_i I_i + \sum_{j \neq i}^{n} m_{ij} I_j - \sum_{j \neq i}^{n} m_{ji} I_i - (\gamma + \delta_i) I_i \\
\frac{dR}{dt} &= \gamma \sum_{i=1}^{n} \delta_i I_i
\end{aligned} \tag{6}$$

When the migration rate is constant among locations and the model is a location-independent SIR model, or equivalently, LIBDS, equation set 6 reduces to

$$\begin{aligned}
\frac{dS_i}{dt} &= -\frac{\beta}{N_i} S_i I_i \\
\frac{dI_i}{dt} &= \frac{\beta}{N_i} S_i I_i + m \left(\sum_{j \neq i}^{n} I_j - (n-1) I_i \right) - (\gamma + \delta) I_i \\
\frac{dR}{dt} &= (\gamma + \delta) \sum_{i=1}^{n} I_i
\end{aligned}$$

The number of infections and the migration of susceptible individuals is at negligible levels on the timescales investigated here. The infection rate is, therefore,

approximately constant and the migration of susceptible individuals can be safely ignored requiring only migration of infectious individuals to be simulated.

At the beginning of an outbreak, it is often easier to know the recovery period from clinical data than the sampling rate which requires knowing the prevalence of the disease. Therefore, we treat the average recovery period as a known quantity and use it to make the other two parameters (the sampling rate and the basic reproduction number R_0) identifiable. This was done by fixing the corresponding rate parameter in the likelihood function to the true simulated value for each tree, and by adding the true simulated value to the training data for training the neural network.

Simulated training and validation data sets

Epidemic simulations of the SIR+migration model that approximates the LIBDS process were performed using the MASTER package v. 6.1.2 (Vaughan et al. 2014) in BEAST 2 v. 2.6.6 (Bouckaert et al. 2019). MASTER allows users to simulate phylodynamic data sets under user-specified epidemiological scenarios, for which MASTER simultaneously simulates the evolution of compartment (population type) sizes and tracks the branching lineages (transmission trees in the case of viruses) from which it samples over time. We trained neural networks with these simulated data to learn about latent populations from the shape of sampled and subsampled phylogenies. In addition to the serial sampling process, at the end of the simulation 1% of infected lineages were sampled. In MASTER this was approximated by setting a very high sampling rate and very short sampling time such that the expected number sampled was approximately 1%. This final sampling event was required to make a 1-to-1 comparison of the likelihood function used for this study (see Likelihood method description below) which assumes at least one extant individual was sampled to end the process. Coverage statistics from our MCMC samples closely match expectations (see Likelihood method description below; SI Figure S2). Simulation

parameters under LIBDS and LDBDS models for training the neural network under the phylogeography model were drawn from the following distributions:

$$\begin{aligned} R_0 &\sim \text{Uniform}(2,\ 8) \\ \delta &\sim \text{Unif}(0.0001,\ 0.005) \\ m &\sim \text{Uniform}(0.0001,\ 0.005) \\ \gamma &\sim \text{Unif}(0.01,\ 0.05) \\ \text{root location} &\sim \text{Multinomial}(\text{k} = 1,\ \text{p}_i = 1/n),\ \text{for } n \text{ locations} \end{aligned} \tag{7}$$

All five locations had initial population sizes of 1,000,000 susceptible individuals and one infected individual in one of the locations. Simulations were run for 100 time units or until 50,000 individuals had been infected to restrict simulations to the approximate exponential phase of the outbreak. For the experiments comparing the CNN to the likelihood-based method under the LIBDS model, if this population threshold was reached the simulation was rejected. This criterion was not enforced for simulations under the LDBDS model. This ensured the LIBDS model used in the likelihood-based analyses are equivalent to more complex density-dependent SIR models. After simulation, trees with 500 or more tips were uniformly and randomly downsampled to 499 tips and the sampling proportion was recorded for training the neural networks and to adjust estimates of δ.

We simulated 410,000 outbreaks under these LIBDS settings to generate the training, validation, and test sets for deep learning. Any simulation that generated a tree with less than 20 tips was discarded, leaving a total of 111,157 simulated epidemiological data sets. Of these, 104,157 data sets were used to train and 7,000 were used to validate and test each CNN. A total of 193,110 LDBDS data sets were simulated, with 186,110 used to train and 7,000 used to validate and test the LDBDS CNNs.

Training simulation parameters for the LDBDS process used to analyze the real

data set (Nadeau et al. 2021) were drawn from the same distributions as LIBDS except R_0 was unique for each location and was drawn from a hierarchical distribution to narrow the magnitude of differences among locations within simulations to be within 8 of each other but expand the magnitude of differences between simulations to range from 0.9 to 15:

$$\alpha \sim \text{Uniform}(4.9,\ 11)$$

$$R_{0_i} \sim \text{Uniform}(\alpha\ \text{-}\ 4,\ \alpha\ +\ 4)$$

For the empirical analysis, population sizes at each location were also set to 500,000 and instead of running the simulations for 100 time units, time was scaled by the recovery period, $1/\gamma$, and was drawn from a uniform distribution:

$$\text{time} \sim \text{Uniform}(1,\ 20)$$

Simulated test data sets with and without model misspecification

We first simulated a test set of 138 trees under the training model to compare the accuracy of the CNN and the likelihood-based estimates when the true model is specified. These data sets were simulated by random draws of parameter values from the same distributions described above for generating the training data set.

Sensitivity to model misspecfication for each of the three rate parameters, R_0, δ, and m, was tested. All sensitivity experiments used the same LIBDS model for inference for both the CNN and the Likelihood-based methods. Sensitivity experiments we conducted by simulating a test data set of trees that were generated by an epidemic process that was more complex than or different from the LIBDS model.

The tree data set for the misspecified R_0 experiment consisted of simulating outbreaks where each location had a unique R_0 drawn from the same distribution as above. Likewise, the misspecified sampling model test set was generated by simulating outbreaks where each location had a unique sampling rate, δ, drawn from the same distribution used for the global sampling rate described above. For the misspecified migration model, a random pair of coordinates, each drawn from a uniform(0,5) distribution in a plane, were generated for the five locations, and a pairwise migration rate was computed such that pairwise migration rates were symmetric and proportional to the inverse of their euclidean distances and the average pairwise migration rate was equal to a random scalar which was also drawn from a uniform distribution (see equations 7 above).

The tree set for the misspecified number of locations experiment was generated by simulating outbreaks among ten locations instead of five. After simulations, six locations were chosen at random and re-coded as being sampled from the same location.

To generate a test set where the time tree used for inference has incorrect topology and branch lengths, we implemented a basic pipeline of tree inference from simulated genetic data to mimic a worst case real world scenario. We simulated trees under the same settings as before. Phylogenetic error was introduced in two ways: the amount of site data (short sequences) and misspecification of the DNA sequence evolution inference model (*i.e.*. Using seq-gen V. 1.3.2 (Rambaut and Grassly 1997). We simulated the evolution of a 200 base-pair sequence under an HKY model with $\kappa = 2$, equal base frequencies and 4 discretized-gamma(2, 2) rate categories for among site rate variation. The simulated alignment as well as the true tip dates (sampling times) was then used to infer test trees. Test tree inference was done using iqtree v. 2.0.6 (Minh et al. 2020) assuming a Jukes-Cantor model of evolution where all transition rates are equal. The inference model also assumed no among-site rate variation. The number of shared branches between the true transmission tree and the test tree inferred by IQ-Tree was measured using gotree v. 0.4.2 (Lemoine and Gascuel 2021). Polytomies were resolved using phytools (Revell 2012)

and a small, random number was added to each resolved branch. These trees were then used for likelihood inference and CNN prediction.

Deep learning inference method

The resulting trees and location metadata generated by our pipeline were converted to a modified cblv format (Voznica et al. 2022), which we refer to as the cblv+S (+State of character, *e.g.* location) format. The cblv format uses an in-order tree traversal to translate the topology and branch lengths of the tree into an 2 x n matrix where n is the number of tips in the tree. This representation gives each sampled tip a pair of coordinates in 'tree-traversal space'. Our cblv+S format associates geographic information corresponding with each sampled taxon by appending each vector column with a one-hot encoding vector of length g states to yield a $(2 + g) \times n$ cblv+S matrix. The cblv+S format allows for multiple characters and/or states to be encoded, extending the single binary character encoding format introduced by Lambert et al. (2022). Our study uses cblv+S to encode a single character with $g = 5$ location-states. In addition to the the cblv+S data, we also include a few tree summary statistics and known simulating parameters; the mean branch length, the tree height and the recovery rate and the subsampling proportion. Trees were rescaled such that their mean branch length was the default for phylodeep (Voznica et al. 2021) before training and testing of the CNN. The mean pre-scaling branch length and tree heights were also fed into the neural networks. Trees were not rescaled for the likelihood-based analysis. Note that tree height did not vary for the LIBDS CNN training set but did for the LDBDS training set.

Our CNNs were implemented in Python 3.8.10 using keras v. 2.6.0 and tensorflow-gpu v. 2.6.0. (Chollet; Abadi et al. 2016). For each model, LIBDS and LDBDS, we designed and trained two CNN architectures, one to predict epidemiological rate parameters and the other to predict the outbreak location resulting in four total CNNs trained by two training data sets (LIBDS and LDBDS). We used the mean-squared-error

for the regression neural loss function in the network trained to estimate epidemiological rates, and the categorical cross-entropy loss function for the categorical network trained to estimate outbreak location. We assessed the performance of the network by randomly selecting 5,000 samples for validation before each round of training. We measured the mean absolute error and accuracy using the validation sets. We used these measures to compare architectures and determine early stopping times to avoid overfitting the model to the training data. We also added more simulations to the training set until we could no longer detect an improvement in error statistics. After comparing the performance of several networks, we found that the CNN described in SI Figure S1 performed the best. In brief, the networks have three parallel sets of sequential convolutional layers for the cblv+S tensor and a parallel dense layer for the priors and tree statistics. The three sets of convolution layers differed by dilation rate and stride lengths. These three segments and the dense layer were concatenated and then fed into a segment consisting of a sequential set of dense layers, each layer gradually narrowing to the output size to either three or five for the rates and origin location networks, respectively, for the LIBDS model, and seven and five for the seven rates and five locations, respectively, for the LDBDS model.

All layers of the CNN used rectified linear unit (ReLU) activation functions. We used the Adam optimizer algorithm for batch stochastic gradient descent (Kingma and Ba 2017) with batch size of 128 and stopping after 15 epochs for the regression network and ten epochs for the root location network. The output activation for the rates network was linear with three nodes and for the outbreak location network was softmax with five nodes. Otherwise the architecture was the same for all four networks. The LDBDS neural network was trained with simulated trees where R_{0_i} varied among locations had output layer with seven nodes; five for the each location's R_{0_i} and a node each for the sampling rate and the migration rate. We tested networks with max-pooling layers between convolution layers as well as dropout at several rates and found no improvement or a decrease in performance.

Likelihood-based method of inference

We compared the performance of our trained phylodynamic CNN to likelihood-based Bayesian phylodynamic inferences. We specified LIBDS and LDBDS Bayesian models that were identical to the LIBDS and LDBDS simulation models that we used to train our CNNs. The most general phylodynamic model in the birth-death family applied to epidemiolgoical data is the state-dependent birth-death-sampling process (SDBDS; (Kühnert et al. 2016; Scire et al. 2020)), where the state or type on which birth, death, and sampling parameters are dependent is the location in this context. The basic model used for experiments here is a phylogeographic model that is similar to the serially sampled birth-death process (Stadler 2010) where rates do not depend on location, which we refer to as the LDBDS model. The death rate, μ, is equivalent to the recovery rate, γ, in SIR models. Standard phylogenetic birth-death models assume the birth and death rates, λ and μ, are constant or time-homogeneous, while the SIR model's infection rate is proportional to β and S and varies with time as S changes. However, when the number of infected is small relative to susceptible people, as in the initial stages of an outbreak, the infection rate, β, is approximately constant and approximately equal to the birth rate λ;

$$\lambda = \frac{\beta S}{N} \approx \beta \tag{8}$$

The joint prior distribution was set to the same model parameter distributions that were used to simulate the training and test sets of phylogenetic trees in the first section with γ treated as known and the proportion of extant lineages sampled, ρ, set to 0.01 as in the simulations. The likelihood was conditioned on the tree having extant samples (*i.e.* the simulation ran for the allotted time without being rejected). All simulated trees in this study had a stem branch and the outbreak origins were inferred for the parent node of the stem branch.

We used Markov chain Monte Carlo (MCMC) to simulate random sampling from the posterior distribution implemented in the TensorPhylo package (https://bitbucket.org/mrmay/tensorphylo/src/master/) in RevBayes (Höhna et al. 2016). After a burnin phase, a single chain was run for 7,500 cycles with 4 proposals per cycle and at least 100 effective sample size (ESS) for all parameters. If the effective sample size (ESS) was less than 100, the MCMC was rerun with a higher number of cycles. We also analyzed the coverage of the 5, 10, 25, 50, 75, 90, and 95% highest posterior density (HPD) intervals to verify that our simulation model and inference model are the same and that the MCMC simulated draws from the true posterior distribution. Bayesian phylogeographic analysis recovered the true simulating parameters (SI Figure S2) at the expected frequencies, thus validating the simulations were working as expected and confirming that the MCMC was accurately simulating draws from the true posterior distribution.

Quantifying errors and error differences

We measure the absolute percent error (APE) of the predictions from the CNN and the mean posterior estimate (MPE) of the likelihood-based method. The formula for APE of a prediction/estimate, y^{estimate}, of y^{truth} is

$$\text{APE} = \left| \frac{y^{\text{estimate}} - y^{\text{truth}}}{y^{\text{truth}}} \right| \times 100$$

The Bayesian alternative to significance testing is to analyze the posterior distribution of parameter value differences between groups. In this framework, the probability that a difference is greater than zero can be easily interpreted. We therefore used Bayesian statistics to infer the median difference in error between the CNN and likelihood-based methods and the increase in median error of each method when analyzing misspecified data compared to when analyzing data simulated under the true inference model.

We used Bayesian inference to quantify population error by performing three sets of analyses: (1) inferred the population median APE under the true model (this will be the reference group for analysis 3), (2) the effect of inference method — CNN or likelihood-based (Bayesian) — on error by inferring the median difference between the CNN estimate and the likelihood-based estimate, (3) the effect of misspecification on error for each parameter by comparing the median error of estimates under misspecified experiments and the reference group defined by analysis 1. See SI Figures S3 - S8 and SI Table S1 for summaries and figures for all analyses for this section.

To infer these differences between groups we used the R package `BEST` (Meredith and Kruschke). BEST assumes the data follow a t-distribution parameterized by a location parameter, μ, a scale parameter, σ, and a shape parameter, ν, which they call the "normality parameter" (*i.e.* if ν is large the distribution is more Normal). Because the posterior distribution does not have a closed form, BEST uses Gibbs sampling to simulate draws from the posterior distribution. 20,000 samples were drawn from the posterior distribution for each BEST analysis. BEST uses automatic posterior predictive checks to indicate that a model adequately describes the data distributions. Posterior predictive checks indicate the BEST model adequately fits each data set analyzed below.

Inferring the median APE.— Before inferring differences between groups, we inferred the population median APE for predictions of R_0, δ, and m from test data simulated under the inference model using the CNN and likelihood-based methods. Histograms of the sampled log-transformed APE appears to be symmetric with heavy tails so we fit the log APE to the BEST model. This implies that the sampled APE scores are drawn from a log-t distribution. The log-t distribution has a mean of ∞ and median of e^{μ}, we therefore focus our inference on estimating posterior intervals for the population median APE from the sampled APE values for each parameter estimated by the CNN method and likelihood-based method which we denote APE^{CNN}, and APE^{Like} respectively. The data

analyzed here and likelihood assumed by BEST is

$$y = \text{APE}^{\text{CNN}} \text{ or } \text{APE}^{\text{Like}}$$
$$\log y \mid \mu, \sigma, \nu \sim t_\nu(\mu, \sigma).$$

The priors were set to the vague priors that BEST provides by default,

$$\mu \sim \text{Normal}(\text{mean(y)}, \text{sd(y)} \times 1000)$$
$$\sigma \sim \text{Uniform}(\text{sd(y)}/1000, \text{ sd(y)} \times 1000)$$
$$\nu \sim \text{Exponential}(1/29) + 1.$$

95% highest posterior intervals (HPI) for the median APE, $\tilde{\mu}$, was estimated by the following transformation of simulated draws from the posterior distribution

$$\tilde{\mu} = e^{\mu}.$$

In summary, the results we present are 95% HPI from the posterior distributions of the median error, $\tilde{\mu}$.

Inferring the relative accuracy of the CNN and likelihood-based method.— To quantify the difference in error between the CNN and the likelihood-based method, we fit the difference in sampled APE scores, ΔAPE, between the CNN method and the likelihood-based method to the BEST model. Histograms of ΔAPE appear symmetric with weak to strong outliers making the BEST model a good candidate for inference from this data. The data and likelihood are

$$\Delta y = \text{APE}^{\text{CNN}} - \text{APE}^{\text{Like}}$$
$$\Delta y \mid \mu, \sigma, \nu \sim t_\nu(\mu, \sigma)$$

We used the same default priors as above.

Because, Δy is not log-transformed, it is drawn from a t-distribution and the marginal posterior of the parameter μ is an estimate of the population mean, μ^d. Because the mean and the median are equivalent for a t-distribution, we again report the posterior distribution of the median difference, $\tilde{\mu}^d$ to simplify the results.

In summary, the results we present are 95% HPI from the posterior distribution of the median difference between the two methods, $\tilde{\mu}^d$.

When comparing CNN to the likelihood-based approach, positive values for $\tilde{\mu}^d$ indicate the CNN is less accurate, and negative indicate the likelihood-based estimates less accurate. We emphasise that this quantity is the median difference in contrast to the difference in medians, $\Delta\tilde{\mu}$, reported in the next section.

Inferring sensitivity to model misspecification.— Finally, to quantify the overall sensitivity of each rate parameter to model misspecification under each inference method, we infer the difference in median APE, $\tilde{\mu}$ of predictions under a misspecified model relative to predictions under the true model. In other words we are inferring differences in medians between experiments. For example, to infer the sensitivity of the CNN's inference of the sampling rate, δ, to phylogenetic error, we inferred the difference between the median APE of the CNN's predictions for misspecified trees and the median APE of CNN predictions for true trees. The data is concatenated as below.

$$(y_1, y_2) = (\text{APE}^{\text{CNN}}, \text{APE}^{\text{CNN Ref}}) \text{ or}$$
$$(y_1, y_2) = (\text{APE}^{\text{Like}}, \text{APE}^{\text{Like Ref}})$$

We inferred the difference between group median APE scores, denoted $\Delta\tilde{\mu}$, by assuming that the model parameters conditioned on the observed APE from the two groups, y_1 and y_2, follow a posterior distribution that is proportional to

$$P(y_1 \mid \mu_1, \sigma_1, \nu)P(y_2 \mid \mu_2, \sigma_2, \nu)P(\mu_1, \mu_2, \sigma_1, \sigma_2, \nu),$$

where $\log y_1$ and $\log y_2$ follow t distributions with means μ_1 and μ_2 and standard deviations σ_1 and σ_2, respectively while sharing a common normality parameter, ν.

The posterior sample of $\Delta\tilde{\mu}$ is obtained by transforming samples from the joint marginal posterior distribution of μ_1 and μ_2 with the following equation,

$$\Delta\tilde{\mu} = e^{\mu_1} - e^{\mu_2}.$$

The two components of the likelihood are each t-distributed and share the ν parameter which means we assume both samples are drawn from a similarly shaped distribution (similarly heavy tails).

$$\log y_1 \mid \mu_1, \sigma_1, \nu \sim t_\nu(\mu_1, \sigma_1)$$
$$\log y_2 \mid \mu_2, \sigma_2, \nu \sim t_\nu(\mu_2, \sigma_2)$$

The prior distribution for the parameters of the model were set to the defaults for BEST,

$$\mu_1 \sim \text{Normal}(\text{mean}(\log y_1), \text{sd}(\log y_1) \times 1000)$$
$$\mu_2 \sim \text{Normal}(\text{mean}(\log y_2), \text{sd}(\log y_2) \times 1000)$$
$$\sigma_1 \sim \text{Uniform}(\text{sd}(\log y_1)/1000, \text{sd}(\log y_1) \times 1000)$$
$$\sigma_2 \sim \text{Uniform}(\text{sd}(\log y_2)/1000, \text{sd}(\log y_2) \times 1000)$$
$$\nu \sim \text{Exponential}(1/29) + 1$$

As before, interpretation of the posterior distribution of the difference in medians is straightforward: the more positive the difference in median APE from the misspecified model test set and the median APE from the true model test set, the more sensitive the parameter is to model misspecification in the experiment.

Real Data

We compared the inferences of a LDBDS simulation trained neural network to that of a phylodynamic study of the first COVID wave in Europe (Nadeau et al. 2021). These authors analyzed a phylogenetic tree of viruses sampled in Europe and Hubei, China using a location-dependent birth-death-sampling model in a Bayesian framework using priors informed by myriad other sources of information. We simulated a new training set of trees under an LDBDS model where R_{0_i} depends on the geographic location, and the sampling process only consists of serial sampling and no sampling of extant infected individuals. We then analyzed the whole tree from Fig. 1 in (Nadeau et al. 2021) as well as the European clade which Nadeau et al. (2021) labeled as A2 in the same figure. We note that our simulating model is not identical to the inference model used in (Nadeau et al. 2021). We model migration with a single parameter with symmetrical migration rates among locations and all locations having the same sample rate. Nadeau and colleagues parameterize the migration process with asymmetric pairwise migration rates and assume location-specific sampling rates. We also do not include the information the authors used to inform their priors as that requires an extra level of simulation and training on top of simulations done here, and is thus beyond the scope of this study.

The time tree from (Nadeau et al. 2021) was downloaded from GitHub (https://github.com/SarahNadeau/cov-europe-bdmm). The recovery rate assumed in (Nadeau et al. 2021) was 0.1 days^{-1} which was set to 0.05 to bring the recovery rate to within the range of simulating values used to train the CNN. Consequently, the branch lengths of the tree were then scaled by 2. The number of tips, tree height, and average

branch lengths were measured from the rescaled trees and fed into the network. The full tree and A2 clade were then analyzed using the LDBD CNN and compared to the posterior distributions from (Nadeau et al. 2021).

Hardware used

Simulations were run on a 16 core Intel(R) Xeon(R) Platinum 8175M CPU @ 2.50GHz. For each simulation, an XML file with random parameter settings was generated using custom scripts. These XML files were the inputs for MASTER which was run in the BEAST2 platform. Neural network training and testing and predictions were conducted on an 8 core Intel(R) Core(TM) i7-7820HQ CPU @ 2.90GHz laptop.

Data and code availability.— A repository containing data and code used in this study is available here: Link to be provided soon.

Results

Comparing deep learning to likelihood

Our first goal in this study was to train a CNN that produced phylodynamic parameter point estimates that were as accurate as likelihood-based Bayesian posterior mean estimates under the true model. This will serve as a reference for quantifying level of sensitivity in our misspecification experiments. We focused on estimating important epidemiological parameters – the reproduction number, R_0, the sampling rate, δ, and the migration rate, m – as well as the outbreak origin from viral phylogenies like those typically estimated from serially sampled DNA sequences that were obtained as the virus spread.

Our CNN produced estimates that are as accurate as the mean posterior estimates (MPE) under the true simulating model. We compared the absolute percent error (APE)

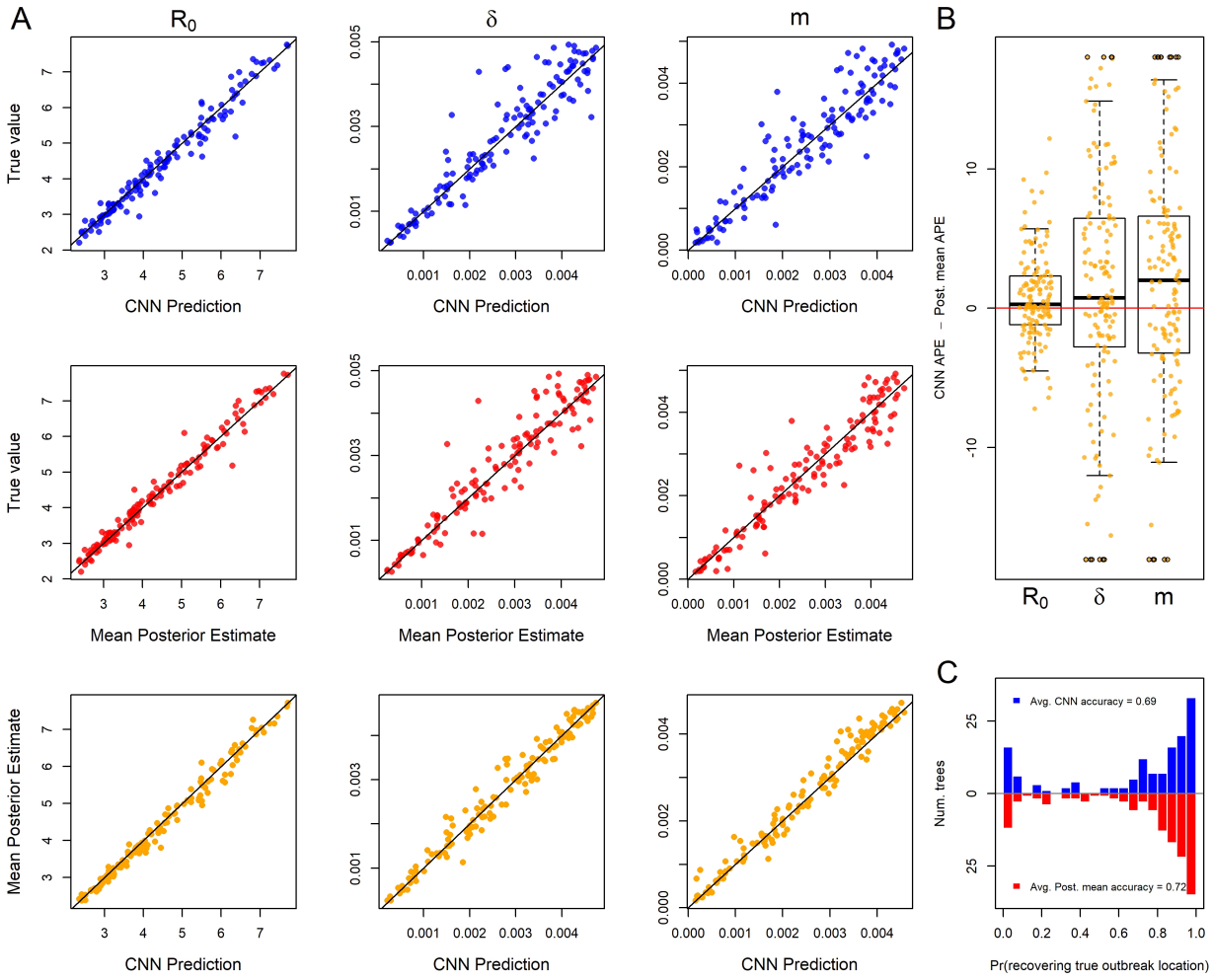

Figure 1: Inference under the true simulating model. (A) Scatterplot of CNN predictions and posterior mean estimates from Bayesian analyses against the true values (top two rows in blue and red respectively) of the basic reproduction number, R_0, the sampling rate, δ, and the migration rate, m for 138 test trees. The bottom row in orange shows scatter plots of the CNN estimates against the posterior mean estimates for the same trees. (B) The difference in the absolute percent error (APE) of estimates for the two inference methods. Boxes show the inner 50% quantile of the data while whiskers extend 1.5 IQR. Dots with black circles show estimates that were truncated to the mean of the parameter with the most extreme outliers for visualization purposes. (C) Histograms of the probabilities of inferring the correct outbreak origin location for the same trees as in panels A and B.

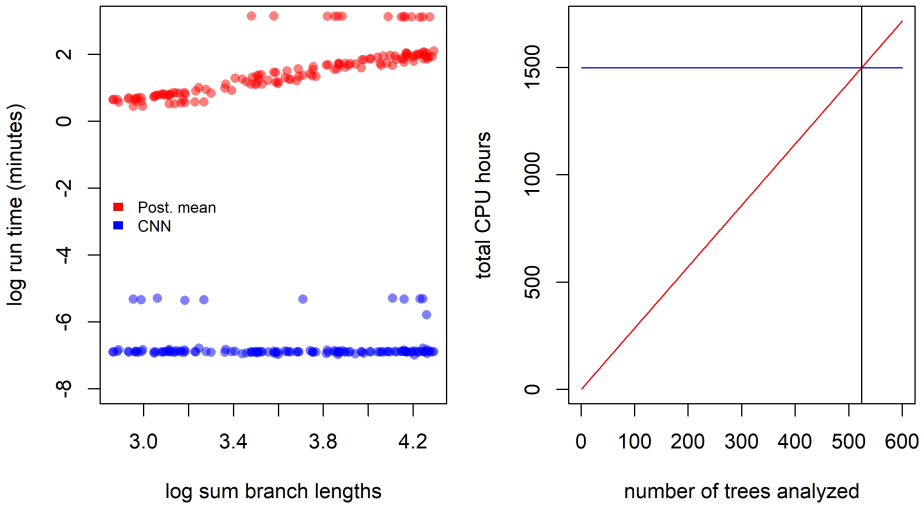

Figure 2: Left: Estimates of time to complete analysis of each of 138 trees relative to tree size. Right: The number of trees (524; gray vertical line) needed to analyze for total analysis time of Bayesian method (red line) to equal that of the entire simulation and CNN training and inference pipeline (blue line).

of the network predictions to the APE of the MPE of the Bayesian LIBDS model (Figure 1). The APE is straight-forward to interpret, e.g. an APE of < 10 means the estimate is within 10 percentage points (ppts) of the true value. For the three epidemiological rate parameters, R_0, δ and m, both methods made very similar predictions for the 100 time tree test set (Figure 1 panel A). The two methods appear to produce estimates that are more similar to each other than to the ground truth labels (compare bottom row scatter plots in orange to the blue and red scatter plots in panel A). Fig. 1 panel B shows that the inferred median difference in APE, $\tilde{\mu}^d$, between the method's estimates for the three parameters is close to zero ($\mid \tilde{\mu}^d \mid$ 95% highest posterior interval (HPI) is < 4 ppts; SI Table S1; SI Figure S3). Fig. 1 Panel C shows that our predictions of the location of outbreak have similar patterns of accuracy as those from the Bayesian method.

Our trained CNN provides nearly instantaneous estimates of model parameters. While the run time of the likelihood approach employed in this study scales linearly with the size of the tree, the neural network has virtually constant run times that are more than

three orders of magnitude faster. Because simulation-trained neural networks have a one-time cost of simulating the training data set and then training the neural network, these methods are often called amortized-approximators (Bürkner et al. 2022). This means the time savings aren't recouped until a certain number of trees have been analyzed. For example, here over 524 trees would need to be analyzed to realize the cost savings of simulating data and training our neural network (Figure 2). This illustrates the importance of simulation optimization and generality for likelihood-free approaches to inference.

Comparing robustness to model misspecification

To test the relative sensitivity of CNN estimates and the likelihood-based MPE to model misspecification, we simulated several test data sets under different, more complex epidemic scenarios and compared the decrease in accuracy (increase in APE).

Our first model misspecification experiment tested performance when assuming all locations had the same R_0 when, in fact, each location had different R_{0_i} values. The median APE for all three parameters increased to varying degrees (SI Fig. S4 Panel A) compared to the median APE measured in Fig. S3. We found that both methods converged on similar biased estimates for R_0. In both the CNN and Bayesian method, estimates of δ were relatively robust to misspecifying R_0. In contrast, the migration rate showed much more sensitivity to this model violation in both methods with both methods also converging on similarly biased estimates (Figure 3 A). The median difference in error between the two methods is close to zero for all rate parameters ($| \tilde{\mu}^d |$ 95% HPI < 6 ppts; SI Table S1) (SI Figure S4 Panel B). The CNN appears to be slightly more sensitive than the Bayesian approach when predicting the outbreak location. Nevertheless, their distributions are quite similar (Fig. 3 Panel C).

Next, we measured method sensitivity when the sampling process of the test trees violates assumptions in the inference model. In this set, each location had a unique and independent sampling rate, δ, rather than a single δ shared among locations. The median

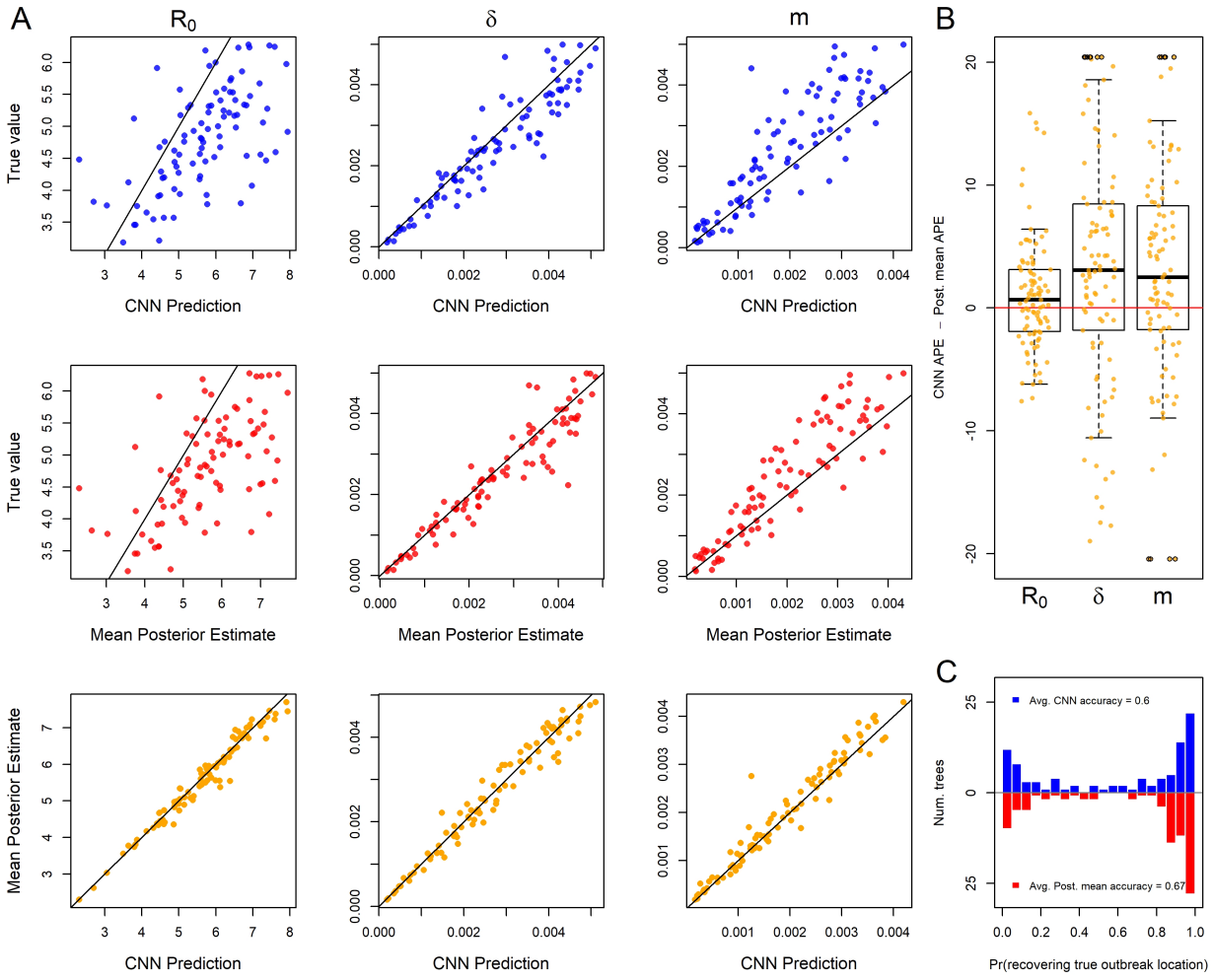

Figure 3: For 93 test trees where the R_0 parameter was misspecified: the simulating model for the test data specified 5 unique R_0s among the five locations while the inference methods assumed one R_0 shared among locations. Because of this, the estimates for R_0 are plotted against mean of the five true R_0 values. See Figure 1 for general details about plots.

APE only increased for δ and m (SI Figure S5 Panel A). As expected, estimates of δ were highly biased for both methods (Figure 4 panel A). Panel A also shows that R_0 is virtually insensitive to sampling model misspecification, but that migration rate, again, is highly sensitive in both the CNN and likelihood method. The median difference in error between the two methods is close to zero for all the rate parameters ($|\ \tilde{\mu}^d\ |$ 95% HPI < 5 ppts; SI Table S1, SI Figure S5) (Figure 4 panel B). The location of outbreak prediction is also somewhat sensitive in both methods, with the CNN showing a slightly larger mean difference, but the overall distribution of accuracy of all the test trees again is similar

(Figure 4 panel C).

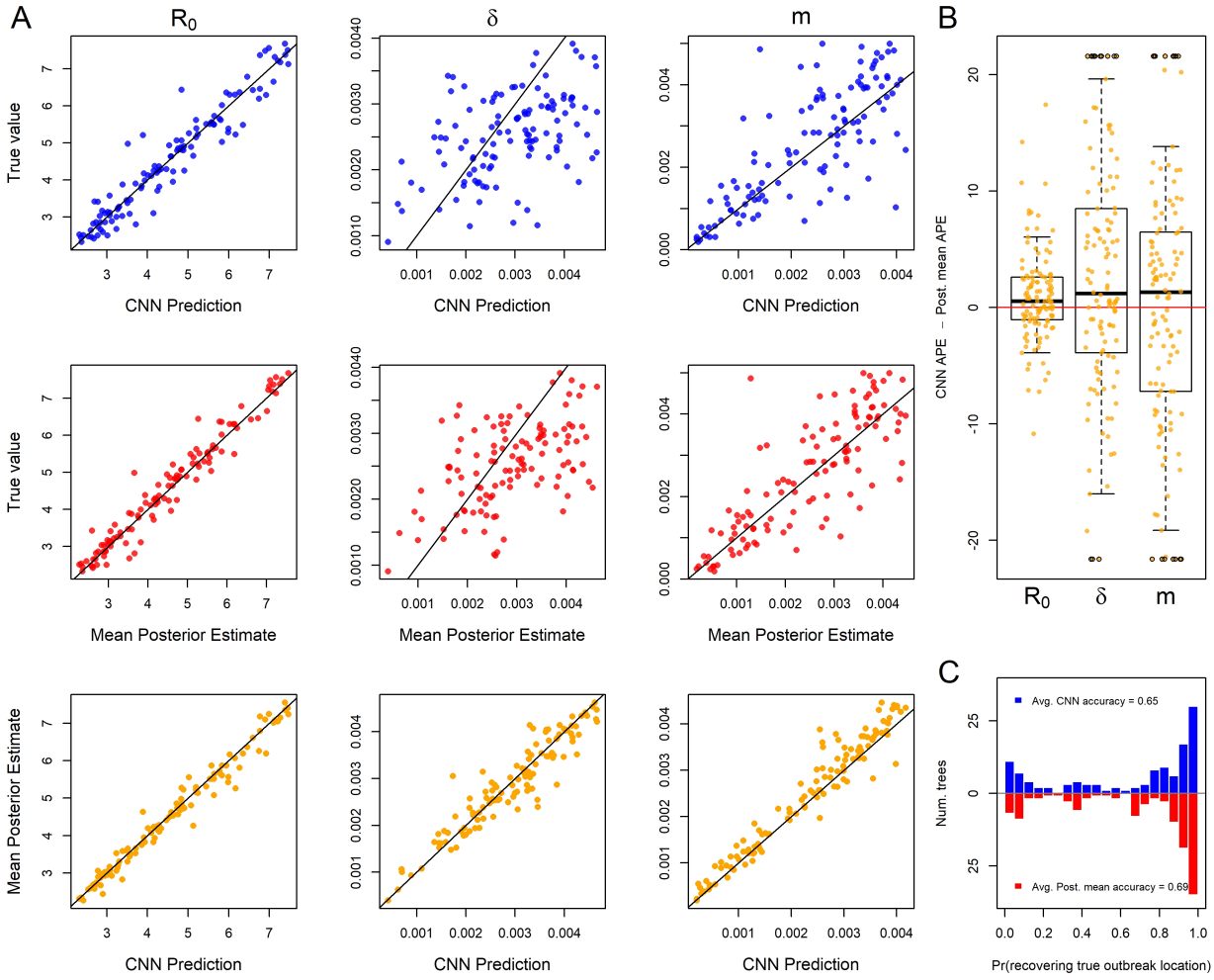

Figure 4: For 118 test trees where the sampling rate parameter was misspecified: the simulating model for the test data specified 5 unique sampling rates among the five locations while the inference methods assumed one sampling rate shared among locations. The estimates of δ are plotted against the mean true values of δ. See Figure 1 for general details about plots.

To explore sensitivity to migration model underspecification, we simulated a test set where the migration rates between locations is free to vary rather than being the same among locations as in the inference model. This implies 5! unique location-pairs and thus unique migration rates in the test data set. Results show that for both methods the parameters R_0 and δ are highly robust to this simplification (SI Fig. S6 Panel A). Though estimates of a single migration rate had a high degree of error compared to a single pair of

locations migration rates (Figure 5 panel A), the two methods still had similar estimates with the difference in APE centered near zero (Figure 5 panel B). The inferred median difference in APE was close to zero ($| \tilde{\mu}^d |$ 95% HPI < 3 ppts; SI Table S1; SI Figure S6 Panel B). There was a slight but similar decrease in accuracy in predicting the outbreak location for both methods (Figure 5 panel C).

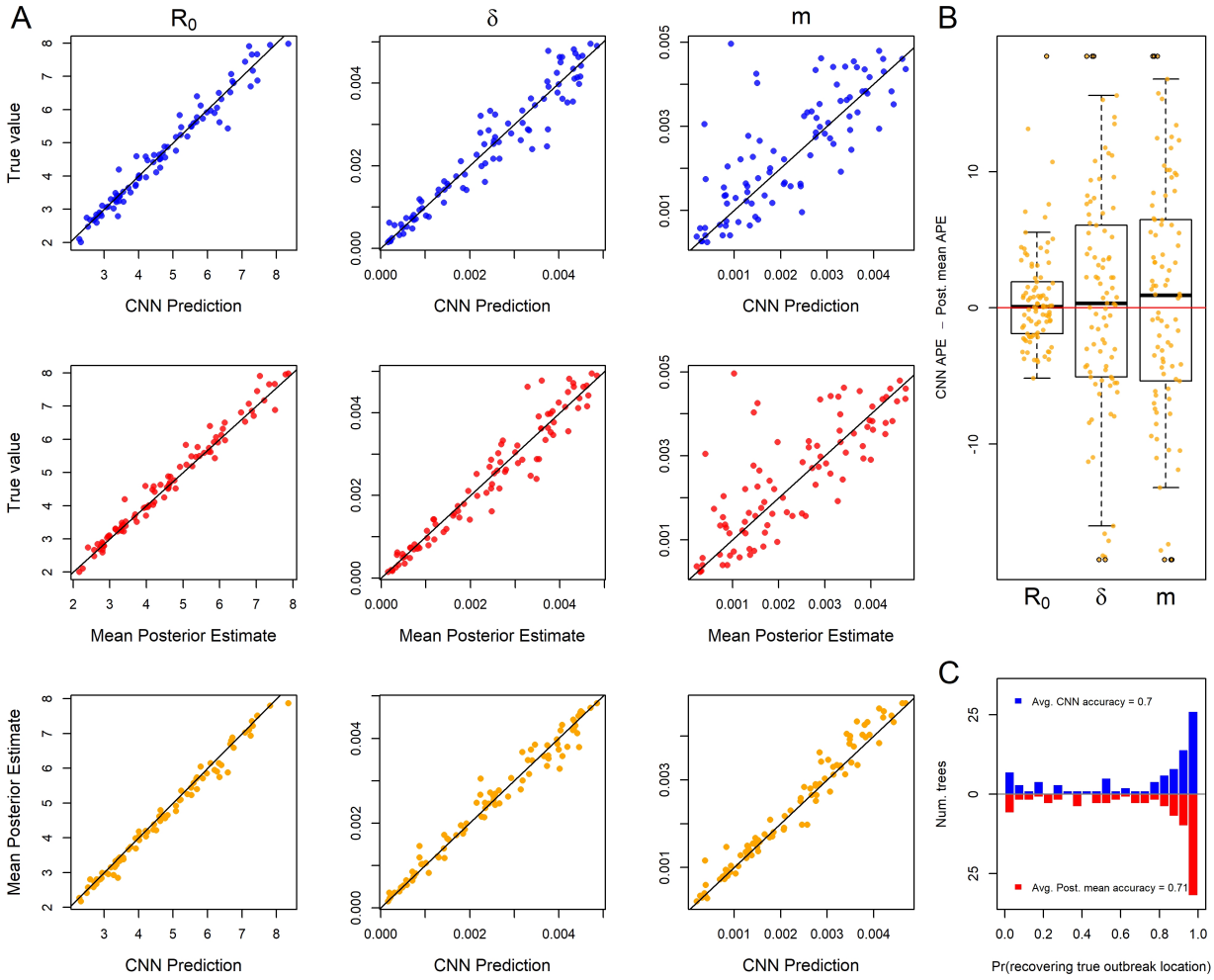

Figure 5: For 90 test trees where the migration rate parameter was misspecified: the simulating model for the test data specified 5! (120) unique migration rates among the unique pairs of the five locations while the inference methods assumed all migration rates were equal. The infered migration rate is plotted against the mean pairwise migraiton rates of test data set. See Figure 1 for general details about plots.

When testing the sensitivity of the two methods to arbitrary groupings of locations, we found that both methods showed equal sensitivity to the same parameters (Fig. 6

Panels A and B). In particular, the migration rate showed a modest increase in median APE and R_0 and sample rate showed virtually no sensitivity to arbitrary grouping of locations (SI Figure S7 Panel A). The inferred median difference between method APE's was again close to zero ($|\ \tilde{\mu}^d\ |$ 95% HPI $<$ 4 ppts; SI Table S1; SI Figure S7 Panel B). This suggests that for at least the exponential phase of outbreaks where rate parameters do not vary among locations, these models have a fair amount of robustness to the decisions leading to geographical division of continuous space into discrete space. The outbreak location showed higher accuracy in both methods due to the fact that the test data was no longer a flat distribution; the 6 combined locations should contain 60% of the outbreak locations (Figure 6 panel C).

Finally, we explored the relative sensitivity of our CNN to amounts of phylogenetic error that are present in typical phylogeographic analyses. Our simulated phylogenetic error produced trees with average normalized Robinson-Foulds distances (Robinson and Foulds 1981) between the inferred tree and the true tree of about 0.5 with 95% of simulated trees having distances within 0.36 and 0.72. We again compared inferences derived from the true tree and the tree with errors using the CNN and the Bayesian LIBDS methods. Results show that migration rate was minimally affected but R_0 and δ were to a some degree sensitive to phylogenetic error (Figure 7 panel A; SI Figure S8 Panel A), with both methods again showing similar degrees of sensitivity (Figure 7 panel B). The inferred median difference was, yet again, small ($|\ \tilde{\mu}^d\ |$ 95% HPI $<$ 6 ppts. SI Table S1, SI Figure S8 Panel B). Inference of the origin location, were very similar for both methods (Fig. 7 Panel C).

Analysis of SARS CoV-2 tree

We next compared our likelihood-free method to a recent study investigating the phylodynamics of the first wave of the SARS CoV-2 pandemic in Europe (Nadeau et al. 2021). Despite simulating the migration and the sampling processes differently from

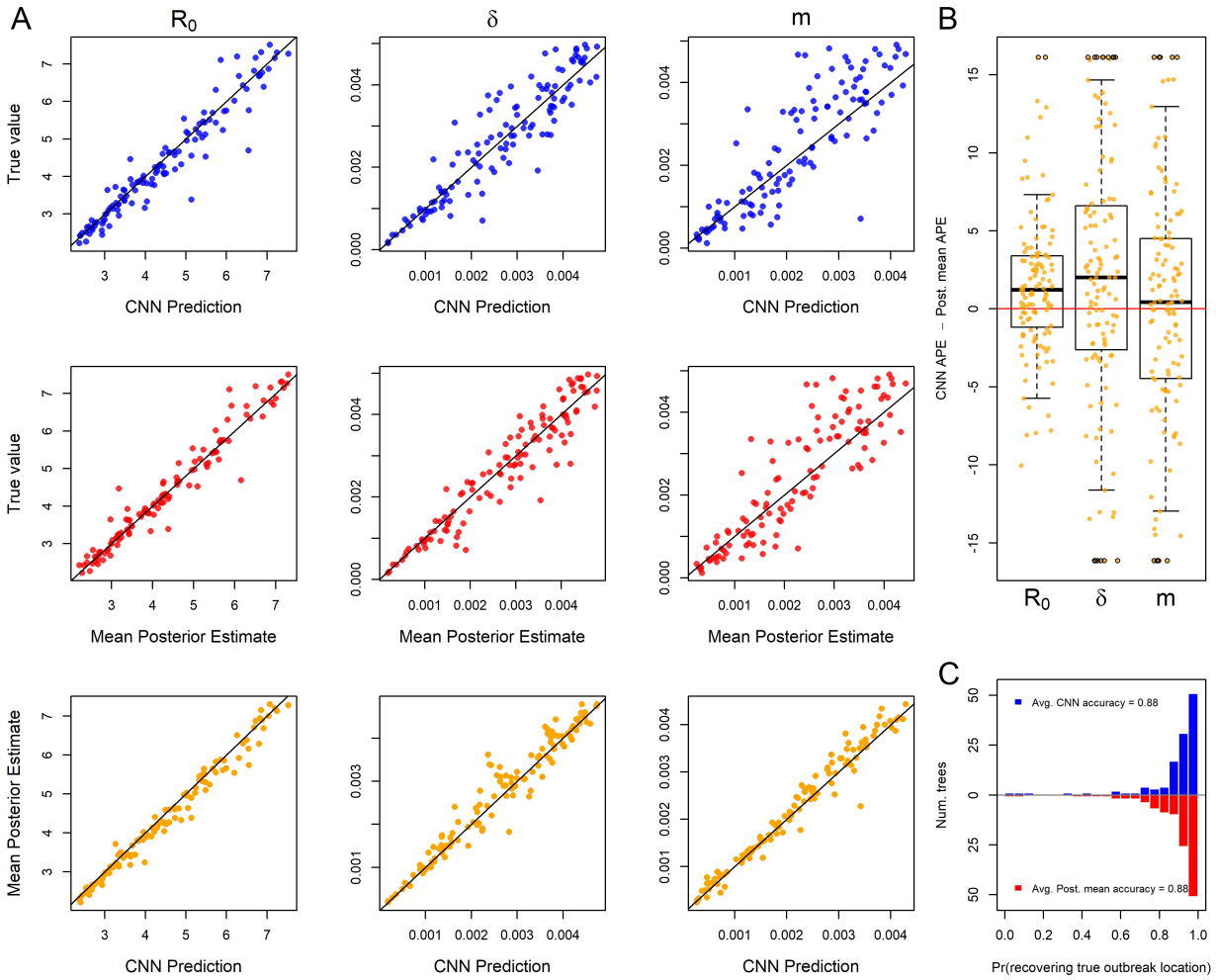

Figure 6: For 101 test trees where the number of locations was misspecified: the simulating model for the test data specified an outbreak among 10 locations with 6 locations subsequently combined into a single location while the inference methods assumed 5 locations with no arbitrary combining of locations. See Figure 1 for general details about plots.

Nadeau et al. (2021), our CNN produces similar estimates for the location-specific R_0 and the origin of the A2 clade (Figure 8). Whether the full tree or just the A2 clade is fed into the network, the predicted R_0 for each location was not far from the posterior estimates of Nadeau et al. (2021). The only significant discrepancy in the origin prediction is that their analysis suggests a much higher probability that the most recent common ancestor of the A2 clade was in Hubei than our CNN predicts. This is likely because our CNN only used the A2 clade to predict A2 origins which has no Hubei samples to infer the origin of the A2 clade while Nadeau et al. (2021) used the whole tree. Notwithstanding this difference,

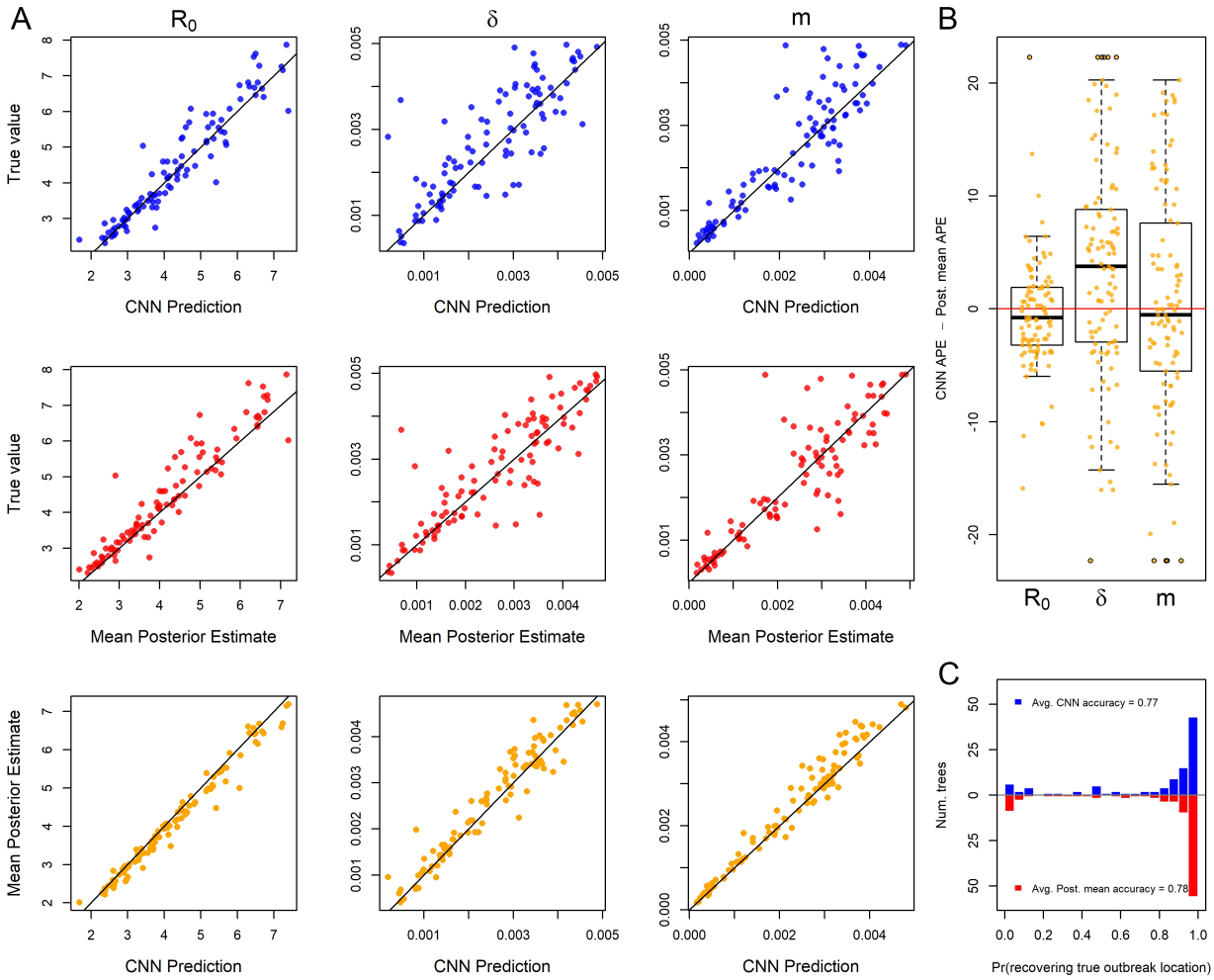

Figure 7: For 118 test trees where the time tree was misspecified: the true tree from the simulated test set was replaced with an inferred tree from simulated DNA alignments under the true tree. See Figure 1 for general details about plots.

among European locations, both methods predict Germany is the most likely location of the most recent common ancestor followed by Italy.

Discussion and Conclusions

Inference models are necessarily a simplified approximation of the real world. Both simulation-trained neural networks and likelihood-based inference approaches suffer from model under-specification and/or misspecification. When comparing inference methods it is important to assess the sensitivity of model inference to simplifying assumptions. In this

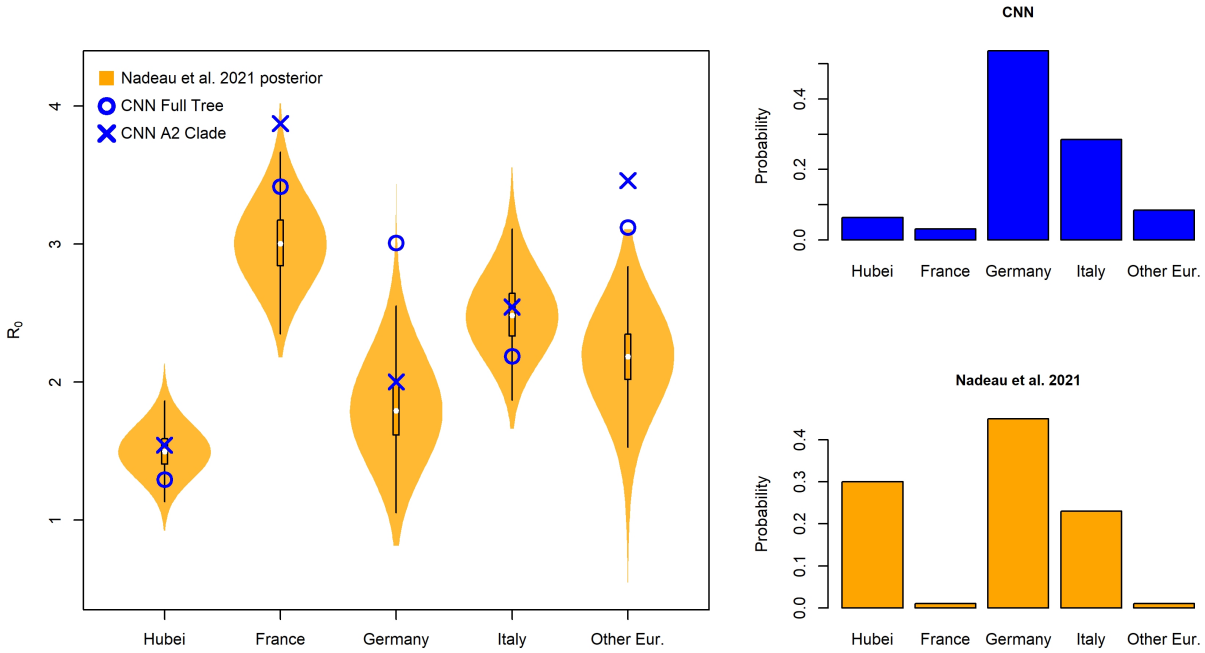

Figure 8: Location-dependent birth-death-sampling model (LDBDS) CNN comparison to (Nadeau et al. 2021) inference. Left violin plots show the posterior distributions of R_0 for each location in Europe as well as Hubei, China (orange). The blue X and O marks the MTBD CNN prediction from analyzing the full tree and the A2 (European) clade respectively. Right barplots show the LDBDS CNN prediction (blue) and posterior inference (orange) from (Nadeau et al. 2021) of the ancestral location of the A2 (European) clade (see Figure 1 (Nadeau et al. 2021)).

study we show that newer deep learning approaches and standard Bayesian approaches behave and misbehave in similar ways under a panel of phylodynamic estimation tasks where the inference model is correct as well as when it is misspecified.

By extending new approaches to encode phylogenetic trees in a compact data structure (Voznica et al. 2021; Lambert et al. 2022), we have developed the first application of phylodynamic deep learning applied to phylogeography with serial sampling. Our approach is similar to that of (Lambert et al. 2022) in which they analyzed a binary SSE model with exclusively extant sampling. By training a neural network on phylogenetic trees generated by simulated epidemics, we were able to accurately estimate key epidemiological parameters, such as the reproduction number and migration rate, in a fraction of the time

it would take with likelihood-based methods. Like Voznica et al. (2021) and Lambert et al. (2022), we found that CNN estimators perform as well or nearly as well as likelihood-based estimators under conditions where the inference model is correctly specified to match the simulation model. The success of these separate applications of deep learning to different phylodynamic problems is a testament to the versatility of the cblv encoding of trees.

We compared the sensitivity of deep learning and likelihood-based inference to model misspecification. Because deep-learning methods of phylogenetic and phylodynamic inference are new, few studies compare how simulation-trained deep learning methods fail in comparison to likelihood methods in this way (Flagel et al. 2019). We assume that when the inference model is correctly specified to match the simulation model, the trained CNN will, at best, produce noisy approximations of likelihood-based parameter estimates. In reality, issues related to training data set size, learning efficiency, and network overfitting may cause our CNN-based estimates to contain excess variance or bias when compared to Bayesian likelihood-based estimators. Our results from five model misspecification experiments show that both methods of inference perform similarly when the simulating model and the inference model assumptions do not perfectly match. These similarities exist not only in aggregate, when comparing method performance across datasets, but also when comparing performance for each individual dataset. This suggests that the CNN and likelihood methods are truly estimating parameters using isomorphic criteria, despite the fact that CNN heuristically learns these criteria through data patterns, while likelihood precisely and mathematically defines these criteria through the model definition itself.

Results of comparative sensitivity experiments like this are important because if likelihood-free methods using deep neural networks can easily be trained to yield estimates that are as robust to model misspecification as likelihood-based methods, then analysis of a large space of more complex outbreak scenarios for which tractable likelihood functions are not available can be developed and applied to real world data. Additionally, sufficiently realistic, pre-trained neural networks can yield nearly instantaneous inferences from data in

real time to inform analysts and policy makers.

We also tested location-dependent SIR simulation trained neural network against a previous publication fitting a similar model – location-dependent birth-death-sampling (LDBDS) model – on real-world data using a Bayesian method. Our CNN predicted location-specific R_{0_i} and outbreak origin in Europe were similar to that inferred in (Nadeau et al. 2021). This result and our model misspecification experiments suggest that simulation-trained deep neural networks trained on phylogenetic trees can find patterns in the training data that generalize well beyond the training data set.

Our study extends the results of Voznica et al. (2022) and Lambert et al. (2022) in several important ways. This work showed that the new compact bijective ladderized vector encoding of phylogenetic trees can easily be extended with one-hot encoding to include metadata about viral samples. We extended it to include location data and were able to train a neural network to not only predict important epidemiological parameters such as R_{0_i} and the sampling rate, but also geographic parameters such as the migration rate and the location of outbreak origination or spillover. We anticipate that much more metadata can be added to train neural networks to bring more diverse and complex data to make predictions about many important aspects of epidemiological spread such as the relative roles of different demographic groups and the overlap of different species' ranges.

This approach can be readily applied to numerous compartment models used to describe the spread of different pathogens among different species, locations, and demographic groups, e.g. SEIR, SIRS, SIS, etc. (Ponciano and Capistrán 2011; Volz and Siveroni 2018; Bjørnstad et al. 2020; Chang et al. 2020; O'Dea and Drake 2021) as well as modeling super-spreader dynamics as in (Voznica et al. 2021). With fast, likelihood-free inference afforded by deep learning, the technical challenges shift from exploring models for which tractable likelihood functions can be derived towards models that produce realistic empirical data patterns, have parameters that control variation of those patterns, and are efficient enough to generate large training data sets. A growing number of advanced

simulators are rapidly expanding the possibilities for deep learning in phylogenetics. For example, FAVITES (Moshiri et al. 2019) is a simulator of disease spread through large contact networks that tracks transmission trees and simulates sequence evolution. Gen3sis, MASTER, SLiM, and VGsim are flexible simulation engines for generating complex ecological, evolutionary, and disease transmission simulations (Hagen et al. 2021; Vaughan and Drummond 2013; Shchur et al. 2021; Haller and Messer 2019; Overcast et al. 2021). Continued advances in epidemic simulation speed and flexibility will be essential for likelihood-free methods to push the boundaries of epidemic modeling sophistication and usefulness.

There are several avenues of development still needed to realize the potential of likelihood-free inference in phylogeography using deep learning. The current setup is ideal for simulation experiments, but it is more difficult to ensure that the optimal parameter values for empirical data sets are within the range of training data parameters. Standardizing input tree height, geographical distance, and other parameters help make training data more universally applicable. Simulation-trained neural networks are often called amortized methods (Bürkner et al. 2022; Schmitt et al. 2022) because the cost of inference is front-loaded, *i.e.* it takes time to simulate a training set and train a neural network. The total cost in time per phylogenetic tree amortizes as the number of trees analyzed by the trained model increases. These methods are therefore important when a model is intended to be widely deployed or be responsive to an emerging outbreak where policy decisions must be formulated rapidly. Because amortized approximate methods require multiple analyses to realize time savings, researchers need to generate training data sets over a broad parameter and model space so that trained networks can be applied to new and diverse data sets. Our research focuses on one phase of an outbreak (the exponential phase), but there are many other scenarios to be investigated, such as when the stage of an epidemic differs among locations (e.g. exponential, peaked, declining).

Quantifying uncertainty is also crucial to data analysis and decision making, and

Bayesian statistics provides a framework for doing so in a rigorous way. Quantifying uncertainty in predictions from deep neural networks is a difficult problem, as these models are trained to minimize prediction error, rather than to explicitly estimate uncertainty. In typical machine learning, uncertainty is ignored or measured using ad hoc methods in which interpretation requires care. Many of these approaches come with their own challenges and limitations, and there is still much ongoing research in this area to address the challenge of quantifying uncertainty in deep neural networks (Gal et al. 2022).

Another important challenge of inference with deep learning is the problem of convergence to a location on the loss function surface that approximates the maximum likelihood well. There are a number of basic heuristics that can help such as learning curves but more rigorous methods of ascertaining convergence is the subject of active research Bürkner et al. (2022); Schmitt et al. (2022).

With recent advances in deep learning in epidemiology, evolution, and ecology (Battey et al. 2020; Schrider and Kern 2018; Voznica et al. 2022; Radev et al. 2021; Lambert et al. 2022; Rosenzweig et al. 2022; Suvorov and Schrider 2022a) biologists can now explore the behavior of entire classes of stochastic branching models that are biologically interesting but mathematically or statistically prohibitive for use with traditional likelihood-based inference techniques. Although we are cautiously optimistic about the future of deep learning methods for phylogenetics, it will become increasingly important for the field to diagnose the conditions where phylogenetic deep learning underperforms relative to likelihood-based approaches, and to devise general solutions for the field.

Funding

National Geospatial-Intelligence Agency. MJL was supported by the National Science Foundation (DEB 2040347) and by an internal grant awarded by the Incubator for Transdisciplinary Futures at Washington University.

Acknowledgements

We are grateful to Fábio Mendes, Sarah Swiston, Sean McHugh, Walker Sexton, and Mariana Braga for helpful comments on the research.

673 *

674 References

675 Martín Abadi, Ashish Agarwal, Paul Barham, Eugene Brevdo, Zhifeng Chen, Craig Citro,
676 Greg S. Corrado, Andy Davis, Jeffrey Dean, Matthieu Devin, Sanjay Ghemawat, Ian
677 Goodfellow, Andrew Harp, Geoffrey Irving, Michael Isard, Yangqing Jia, Rafal
678 Jozefowicz, Lukasz Kaiser, Manjunath Kudlur, Josh Levenberg, Dan Mane, Rajat
679 Monga, Sherry Moore, Derek Murray, Chris Olah, Mike Schuster, Jonathon Shlens,
680 Benoit Steiner, Ilya Sutskever, Kunal Talwar, Paul Tucker, Vincent Vanhoucke, Vijay
681 Vasudevan, Fernanda Viegas, Oriol Vinyals, Pete Warden, Martin Wattenberg, Martin
682 Wicke, Yuan Yu, and Xiaoqiang Zheng. TensorFlow: Large-Scale Machine Learning on
683 Heterogeneous Distributed Systems, March 2016.

684 CJ Battey, Peter L Ralph, and Andrew D Kern. Predicting geographic location from
685 genetic variation with deep neural networks. *eLife*, 9:e54507, June 2020. ISSN
686 2050-084X. doi: 10.7554/eLife.54507.

687 Jeremy M. Beaulieu and Brian C. O'Meara. Detecting Hidden Diversification Shifts in
688 Models of Trait-Dependent Speciation and Extinction. *Systematic Biology*, 65(4):
689 583–601, July 2016. ISSN 1063-5157, 1076-836X. doi: 10.1093/sysbio/syw022.

690 Ottar N. Bjørnstad, Katriona Shea, Martin Krzywinski, and Naomi Altman. The SEIRS
691 model for infectious disease dynamics. *Nature Methods*, 17(6):557–558, June 2020. ISSN
692 1548-7091, 1548-7105. doi: 10.1038/s41592-020-0856-2.

693 Folmer Bokma. Artificial neural networks can learn to estimate extinction rates from
694 molecular phylogenies. *Journal of theoretical biology*, 243(3):449–454, 2006.

695 Remco Bouckaert, Timothy G. Vaughan, Joëlle Barido-Sottani, Sebastián Duchêne,
696 Mathieu Fourment, Alexandra Gavryushkina, Joseph Heled, Graham Jones, Denise

Kühnert, Nicola De Maio, Michael Matschiner, Fábio K. Mendes, Nicola F. Müller, Huw A. Ogilvie, Louis du Plessis, Alex Popinga, Andrew Rambaut, David Rasmussen, Igor Siveroni, Marc A. Suchard, Chieh-Hsi Wu, Dong Xie, Chi Zhang, Tanja Stadler, and Alexei J. Drummond. BEAST 2.5: An advanced software platform for Bayesian evolutionary analysis. *PLOS Computational Biology*, 15(4):e1006650, April 2019. ISSN 1553-7358. doi: 10.1371/journal.pcbi.1006650.

Paul-Christian Bürkner, Maximilian Scholz, and Stefan Radev. Some models are useful, but how do we know which ones? Towards a unified Bayesian model taxonomy, September 2022.

Sheryl L. Chang, Mahendra Piraveenan, Philippa Pattison, and Mikhail Prokopenko. Game theoretic modelling of infectious disease dynamics and intervention methods: A review. *Journal of Biological Dynamics*, 14(1):57–89, January 2020. ISSN 1751-3758, 1751-3766. doi: 10.1080/17513758.2020.1720322.

F. K. Chollet. Keras: The Python deep learning API. https://keras.io/.

Kyle Cranmer, Johann Brehmer, and Gilles Louppe. The frontier of simulation-based inference. *Proceedings of the National Academy of Sciences*, 117(48):30055–30062, December 2020. ISSN 0027-8424, 1091-6490. doi: 10.1073/pnas.1912789117.

Emanuel Masiero da Fonseca, Guarino R. Colli, Fernanda P. Werneck, and Bryan C. Carstens. Phylogeographic model selection using convolutional neural networks, September 2020.

Jordan Douglas, Fábio K Mendes, Remco Bouckaert, Dong Xie, Cinthy L Jiménez-Silva, Christiaan Swanepoel, Joep de Ligt, Xiaoyun Ren, Matt Storey, James Hadfield, Colin R Simpson, Jemma L Geoghegan, Alexei J Drummond, and David Welch. Phylodynamics reveals the role of human travel and contact tracing in controlling the first wave of

721 COVID-19 in four island nations. *Virus Evolution*, 7(2), September 2021. ISSN
722 2057-1577. doi: 10.1093/ve/veab052.

723 Richard G. FitzJohn. Diversitree: Comparative phylogenetic analyses of diversification in
724 R. *Methods in Ecology and Evolution*, 3(6):1084–1092, 2012. ISSN 2041-210X. doi:
725 10.1111/j.2041-210X.2012.00234.x.

726 Lex Flagel, Yaniv Brandvain, and Daniel R Schrider. The Unreasonable Effectiveness of
727 Convolutional Neural Networks in Population Genetic Inference. *Molecular Biology and*
728 *Evolution*, 36(2):220–238, February 2019. ISSN 0737-4038, 1537-1719. doi:
729 10.1093/molbev/msy224.

730 Yarin Gal, Petros Koumoutsakos, Francois Lanusse, Gilles Louppe, and Costas
731 Papadimitriou. Bayesian uncertainty quantification for machine-learned models in
732 physics. *Nature Reviews Physics*, August 2022. ISSN 2522-5820. doi:
733 10.1038/s42254-022-00498-4.

734 Jiansi Gao, Michael R. May, Bruce Rannala, and Brian R. Moore. New Interval-Specific
735 Phylodynamic Models Improve Inference of the Geographic History of Disease
736 Outbreaks, December 2021.

737 Jiansi Gao, Michael R. May, Bruce Rannala, and Brian R. Moore. Model Misspecification
738 Misleads Inference of the Spatial Dynamics of Disease Outbreaks, August 2022.

739 James Hadfield, Colin Megill, Sidney M Bell, John Huddleston, Barney Potter, Charlton
740 Callender, Pavel Sagulenko, Trevor Bedford, and Richard A Neher. Nextstrain: real-time
741 tracking of pathogen evolution. *Bioinformatics*, 34(23):4121–4123, December 2018. ISSN
742 1367-4803. doi: 10.1093/bioinformatics/bty407. URL
743 `https://doi.org/10.1093/bioinformatics/bty407`.

744 Oskar Hagen, Benjamin Flück, Fabian Fopp, Juliano S. Cabral, Florian Hartig, Mikael
745 Pontarp, Thiago F. Rangel, and Loïc Pellissier. Gen3sis: A general engine for

eco-evolutionary simulations of the processes that shape Earth's biodiversity. *PLOS Biology*, 19(7):e3001340, July 2021. ISSN 1545-7885. doi: 10.1371/journal.pbio.3001340.

Benjamin C Haller and Philipp W Messer. SLiM 3: Forward Genetic Simulations Beyond the Wright–Fisher Model. *Molecular Biology and Evolution*, 36(3):632–637, March 2019. ISSN 0737-4038. doi: 10.1093/molbev/msy228.

Sebastian Höhna, Michael J. Landis, Tracy A. Heath, Bastien Boussau, Nicolas Lartillot, Brian R. Moore, John P. Huelsenbeck, and Fredrik Ronquist. RevBayes: Bayesian Phylogenetic Inference Using Graphical Models and an Interactive Model-Specification Language. *Systematic Biology*, 65(4):726–736, July 2016. ISSN 1063-5157, 1076-836X. doi: 10.1093/sysbio/syw021.

Eddie C Holmes and Geoff P Garnett. Genes, trees and infections: molecular evidence in epidemiology. *Trends in Ecology & Evolution*, 9(7):256–260, 1994.

Eddie C Holmes, Sean Nee, Andrew Rambaut, Geoff P Garnett, and Paul H Harvey. Revealing the history of infectious disease epidemics through phylogenetic trees. *Philosophical Transactions of the Royal Society of London. Series B: Biological Sciences*, 349(1327):33–40, 1995.

Diederik P. Kingma and Jimmy Ba. Adam: A Method for Stochastic Optimization, January 2017.

Denise Kühnert, Tanja Stadler, Timothy G. Vaughan, and Alexei J. Drummond. Simultaneous reconstruction of evolutionary history and epidemiological dynamics from viral sequences with the birth–death SIR model. *Journal of The Royal Society Interface*, 11(94):20131106, May 2014. ISSN 1742-5689, 1742-5662. doi: 10.1098/rsif.2013.1106.

Denise Kühnert, Tanja Stadler, Timothy G. Vaughan, and Alexei J. Drummond. Phylodynamics with Migration: A Computational Framework to Quantify Population

770 Structure from Genomic Data. *Molecular Biology and Evolution*, 33(8):2102–2116,
771 August 2016. ISSN 0737-4038. doi: 10.1093/molbev/msw064.

772 Sophia Lambert, Jakub Voznica, and Hélène Morlon. Deep Learning from Phylogenies for
773 Diversification Analyses, September 2022.

774 Philippe Lemey, Andrew Rambaut, Alexei J. Drummond, and Marc A. Suchard. Bayesian
775 Phylogeography Finds Its Roots. *PLoS Computational Biology*, 5(9):e1000520,
776 September 2009. ISSN 1553-7358. doi: 10.1371/journal.pcbi.1000520.

777 Philippe Lemey, Nick Ruktanonchai, Samuel L. Hong, Vittoria Colizza, Chiara Poletto,
778 Frederik Van den Broeck, Mandev S. Gill, Xiang Ji, Anthony Levasseur, Bas B.
779 Oude Munnink, Marion Koopmans, Adam Sadilek, Shengjie Lai, Andrew J. Tatem, Guy
780 Baele, Marc A. Suchard, and Simon Dellicour. Untangling introductions and persistence
781 in COVID-19 resurgence in Europe. *Nature*, June 2021. ISSN 0028-0836, 1476-4687. doi:
782 10.1038/s41586-021-03754-2.

783 Frédéric Lemoine and Olivier Gascuel. Gotree/Goalign: Toolkit and Go API to facilitate
784 the development of phylogenetic workflows. *NAR Genomics and Bioinformatics*, 3(3):
785 lqab075, September 2021. ISSN 2631-9268. doi: 10.1093/nargab/lqab075.

786 Lu Lu, Reina S. Sikkema, Francisca C. Velkers, David F. Nieuwenhuijse, Egil A. J. Fischer,
787 Paola A. Meijer, Noortje Bouwmeester-Vincken, Ariene Rietveld, Marjolijn C. A.
788 Wegdam-Blans, Paulien Tolsma, Marco Koppelman, Lidwien A. M. Smit, Renate W.
789 Hakze-van der Honing, Wim H. M. van der Poel, Arco N. van der Spek, Marcel A. H.
790 Spierenburg, Robert Jan Molenaar, Jan de Rond, Marieke Augustijn, Mark Woolhouse,
791 J. Arjan Stegeman, Samantha Lycett, Bas B. Oude Munnink, and Marion P. G.
792 Koopmans. Adaptation, spread and transmission of SARS-CoV-2 in farmed minks and
793 associated humans in the Netherlands. *Nature Communications*, 12(1):6802, December
794 2021. ISSN 2041-1723. doi: 10.1038/s41467-021-27096-9.

795 Wayne P. Maddison, Peter E. Midford, and Sarah P. Otto. Estimating a Binary
796 Character's Effect on Speciation and Extinction. *Systematic Biology*, 56(5):701–710,
797 October 2007. ISSN 1076-836X, 1063-5157. doi: 10.1080/10635150701607033.

798 Odile Maliet, Florian Hartig, and Hélène Morlon. A model with many small shifts for
799 estimating species-specific diversification rates. *Nature Ecology & Evolution*, 3(7):
800 1086–1092, July 2019. ISSN 2397-334X. doi: 10.1038/s41559-019-0908-0.

801 Mike Meredith and John Kruschke. Bayesian Estimation Supersedes the t-Test. page 13.

802 Bui Quang Minh, Heiko A Schmidt, Olga Chernomor, Dominik Schrempf, Michael D
803 Woodhams, Arndt von Haeseler, and Robert Lanfear. IQ-TREE 2: New Models and
804 Efficient Methods for Phylogenetic Inference in the Genomic Era. *Molecular Biology and*
805 *Evolution*, 37(5):1530–1534, May 2020. ISSN 0737-4038. doi: 10.1093/molbev/msaa015.

806 Niema Moshiri, Manon Ragonnet-Cronin, Joel O Wertheim, and Siavash Mirarab.
807 FAVITES: Simultaneous simulation of transmission networks, phylogenetic trees and
808 sequences. *Bioinformatics*, 35(11):1852–1861, June 2019. ISSN 1367-4803, 1460-2059.
809 doi: 10.1093/bioinformatics/bty921.

810 Sarah A. Nadeau, Timothy G. Vaughan, Jérémie Scire, Jana S. Huisman, and Tanja
811 Stadler. The origin and early spread of SARS-CoV-2 in Europe. *Proceedings of the*
812 *National Academy of Sciences*, 118(9):e2012008118, March 2021. ISSN 0027-8424,
813 1091-6490. doi: 10.1073/pnas.2012008118.

814 Luca Nesterenko, Bastien Boussau, and Laurent Jacob. Phyloformer: Towards fast and
815 accurate phylogeny estimation with self-attention networks, June 2022.

816 Eamon B O'Dea and John M Drake. A semi-parametric, state-space compartmental model
817 with time-dependent parameters for forecasting COVID-19 cases, hospitalizations, and
818 deaths. page 32, 2021.

819 Isaac Overcast, Megan Ruffley, James Rosindell, Luke Harmon, Paulo AV Borges, Brent C
820 Emerson, Rampal S Etienne, Rosemary Gillespie, Henrik Krehenwinkel, D Luke Mahler,
821 et al. A unified model of species abundance, genetic diversity, and functional diversity
822 reveals the mechanisms structuring ecological communities. *Molecular Ecology*
823 *Resources*, 21(8):2782–2800, 2021.

824 Jonathan E. Pekar, Andrew Magee, Edyth Parker, Niema Moshiri, Katherine Izhikevich,
825 Jennifer L. Havens, Karthik Gangavarapu, Lorena Mariana Malpica Serrano, Alexander
826 Crits-Christoph, Nathaniel L. Matteson, Mark Zeller, Joshua I. Levy, Jade C. Wang,
827 Scott Hughes, Jungmin Lee, Heedo Park, Man-Seong Park, Katherine Zi Yan Ching,
828 Raymond Tzer Pin Lin, Mohd Noor Mat Isa, Yusuf Muhammad Noor, Tetyana I.
829 Vasylyeva, Robert F. Garry, Edward C. Holmes, Andrew Rambaut, Marc A. Suchard,
830 Kristian G. Andersen, Michael Worobey, and Joel O. Wertheim. The molecular
831 epidemiology of multiple zoonotic origins of SARS-CoV-2. *Science*, 0(0):eabp8337, July
832 2022. doi: 10.1126/science.abp8337.

833 José M. Ponciano and Marcos A. Capistrán. First Principles Modeling of Nonlinear
834 Incidence Rates in Seasonal Epidemics. *PLOS Computational Biology*, 7(2):e1001079,
835 February 2011. ISSN 1553-7358. doi: 10.1371/journal.pcbi.1001079.

836 O. G. Pybus, M. A. Suchard, P. Lemey, F. J. Bernardin, A. Rambaut, F. W. Crawford,
837 R. R. Gray, N. Arinaminpathy, S. L. Stramer, M. P. Busch, and E. L. Delwart. Unifying
838 the spatial epidemiology and molecular evolution of emerging epidemics. *Proceedings of*
839 *the National Academy of Sciences*, 109(37):15066–15071, September 2012. ISSN
840 0027-8424, 1091-6490. doi: 10.1073/pnas.1206598109.

841 Stefan T. Radev, Frederik Graw, Simiao Chen, Nico T. Mutters, Vanessa M. Eichel, Till
842 Bärnighausen, and Ullrich Köthe. OutbreakFlow: Model-based Bayesian inference of
843 disease outbreak dynamics with invertible neural networks and its application to the

COVID-19 pandemics in Germany. *PLOS Computational Biology*, 17(10):e1009472, October 2021. ISSN 1553-7358. doi: 10.1371/journal.pcbi.1009472.

A. Rambaut and N. C. Grassly. Seq-Gen: an application for the Monte Carlo simulation of DNA sequence evolution along phylogenetic trees. *Computer Applications in the Biosciences*, 13:235–238, 1997.

Andrew Rambaut, Oliver G Pybus, Martha I Nelson, Cecile Viboud, Jeffery K Taubenberger, and Edward C Holmes. The genomic and epidemiological dynamics of human influenza a virus. *Nature*, 453(7195):615–619, 2008.

Liam J. Revell. Phytools: An R package for phylogenetic comparative biology (and other things). *Methods in Ecology and Evolution*, 3(2):217–223, 2012. ISSN 2041-210X. doi: 10.1111/j.2041-210X.2011.00169.x.

Francisco Richter, Bart Haegeman, Rampal S. Etienne, and Ernst C. Wit. Introducing a general class of species diversification models for phylogenetic trees. *Statistica Neerlandica*, 74(3):261–274, 2020. ISSN 1467-9574. doi: 10.1111/stan.12205.

D. F. Robinson and L. R. Foulds. Comparison of phylogenetic trees. *Mathematical Biosciences*, 53:131–147, 1981.

Benjamin K. Rosenzweig, Matthew W. Hahn, and Andrew Kern. Accurate Detection of Incomplete Lineage Sorting via Supervised Machine Learning, November 2022.

Marvin Schmitt, Paul-Christian Bürkner, Ullrich Köthe, and Stefan T. Radev. Detecting Model Misspecification in Amortized Bayesian Inference with Neural Networks, May 2022.

Daniel R. Schrider and Andrew D. Kern. Supervised Machine Learning for Population Genetics: A New Paradigm. *Trends in Genetics*, 34(4):301–312, April 2018. ISSN 01689525. doi: 10.1016/j.tig.2017.12.005.

Jérémie Scire, Joëlle Barido-Sottani, Denise Kühnert, Timothy G. Vaughan, and Tanja Stadler. Improved multi-type birth-death phylodynamic inference in BEAST 2. Preprint, Evolutionary Biology, January 2020.

Vladimir Shchur, Vadim Spirin, Dmitry Sirotkin, Evgeni Burovski, Nicola De Maio, and Russell Corbett-Detig. VGsim: Scalable viral genealogy simulator for global pandemic. Preprint, Epidemiology, April 2021.

Claudia Solis-Lemus, Shengwen Yang, and Leonardo Zepeda-Nunez. Accurate Phylogenetic Inference with a Symmetry-preserving Neural Network Model, January 2022.

Tanja Stadler. Sampling-through-time in birth–death trees. *Journal of Theoretical Biology*, 267(3):396–404, December 2010. ISSN 00225193. doi: 10.1016/j.jtbi.2010.09.010.

Tanja Stadler, Roger Kouyos, Viktor von Wyl, Sabine Yerly, Jürg Böni, Philippe Bürgisser, Thomas Klimkait, Beda Joos, Philip Rieder, Dong Xie, Huldrych F. Günthard, Alexei J. Drummond, Sebastian Bonhoeffer, and the Swiss HIV Cohort Study. Estimating the Basic Reproductive Number from Viral Sequence Data. *Molecular Biology and Evolution*, 29(1):347–357, January 2012. ISSN 1537-1719, 0737-4038. doi: 10.1093/molbev/msr217.

Anton Suvorov and Daniel Schrider. Reliable estimation of tree branch lengths using deep neural networks. *bioRxiv*, 2022a.

Anton Suvorov and Daniel R. Schrider. Reliable estimation of tree branch lengths using deep neural networks, November 2022b.

Anton Suvorov, Joshua Hochuli, and Daniel R Schrider. Accurate Inference of Tree Topologies from Multiple Sequence Alignments Using Deep Learning. *Systematic Biology*, 69(2):221–233, March 2020. ISSN 1063-5157, 1076-836X. doi: 10.1093/sysbio/syz060.

Timothy G. Vaughan and Alexei J. Drummond. A Stochastic Simulator of Birth–Death

Master Equations with Application to Phylodynamics. *Molecular Biology and Evolution*, 30(6):1480–1493, June 2013. ISSN 0737-4038. doi: 10.1093/molbev/mst057.

Timothy G. Vaughan, Denise Kühnert, Alex Popinga, David Welch, and Alexei J. Drummond. Efficient Bayesian inference under the structured coalescent. *Bioinformatics*, 30(16):2272–2279, August 2014. ISSN 1367-4803, 1460-2059. doi: 10.1093/bioinformatics/btu201.

Erik M. Volz and Igor Siveroni. Bayesian phylodynamic inference with complex models. *PLOS Computational Biology*, 14(11):e1006546, November 2018. ISSN 1553-7358. doi: 10.1371/journal.pcbi.1006546.

Erik M. Volz, Katia Koelle, and Trevor Bedford. Viral Phylodynamics. *PLOS Computational Biology*, 9(3):e1002947, March 2013. ISSN 1553-7358. doi: 10.1371/journal.pcbi.1002947. URL `https://journals.plos.org/ploscompbiol/article?id=10.1371/journal.pcbi.1002947`. Publisher: Public Library of Science.

J Voznica, A Zhukova, V Boskova, E Saulnier, F Lemoine, M Moslonka-Lefebvre, and O Gascuel. Deep learning from phylogenies to uncover the epidemiological dynamics of outbreaks. preprint, Bioinformatics, March 2021. URL `http://biorxiv.org/lookup/doi/10.1101/2021.03.11.435006`.

J. Voznica, A. Zhukova, V. Boskova, E. Saulnier, F. Lemoine, M. Moslonka-Lefebvre, and O. Gascuel. Deep learning from phylogenies to uncover the epidemiological dynamics of outbreaks. *Nature Communications*, 13(1):3896, July 2022. ISSN 2041-1723. doi: 10.1038/s41467-022-31511-0.

Nicole L. Washington, Karthik Gangavarapu, Mark Zeller, Alexandre Bolze, Elizabeth T. Cirulli, Kelly M. Schiabor Barrett, Brendan B. Larsen, Catelyn Anderson, Simon White, Tyler Cassens, Sharoni Jacobs, Geraint Levan, Jason Nguyen, Jimmy M. Ramirez,

Charlotte Rivera-Garcia, Efren Sandoval, Xueqing Wang, David Wong, Emily Spencer, Refugio Robles-Sikisaka, Ezra Kurzban, Laura D. Hughes, Xianding Deng, Candace Wang, Venice Servellita, Holly Valentine, Peter De Hoff, Phoebe Seaver, Shashank Sathe, Kimberly Gietzen, Brad Sickler, Jay Antico, Kelly Hoon, Jingtao Liu, Aaron Harding, Omid Bakhtar, Tracy Basler, Brett Austin, Duncan MacCannell, Magnus Isaksson, Phillip G. Febbo, David Becker, Marc Laurent, Eric McDonald, Gene W. Yeo, Rob Knight, Louise C. Laurent, Eileen de Feo, Michael Worobey, Charles Y. Chiu, Marc A. Suchard, James T. Lu, William Lee, and Kristian G. Andersen. Emergence and rapid transmission of SARS-CoV-2 B.1.1.7 in the United States. *Cell*, 184(10):2587–2594.e7, May 2021. ISSN 00928674. doi: 10.1016/j.cell.2021.03.052.

Michael Worobey, Thomas D Watts, Richard A McKay, Marc A Suchard, Timothy Granade, Dirk E Teuwen, Beryl A Koblin, Walid Heneine, Philippe Lemey, and Harold W Jaffe. 1970s and 'patient 0'hiv-1 genomes illuminate early hiv/aids history in north america. *Nature*, 539(7627):98–101, 2016.

Michael Worobey, Jonathan Pekar, Brendan B. Larsen, Martha I. Nelson, Verity Hill, Jeffrey B. Joy, Andrew Rambaut, Marc A. Suchard, Joel O. Wertheim, and Philippe Lemey. The emergence of SARS-CoV-2 in Europe and North America. *Science*, 370 (6516):564–570, October 2020. ISSN 0036-8075, 1095-9203. doi: 10.1126/science.abc8169.

Supplemental Tables and Figures

Table S1: BEST comparisons between CNN and Bayesian absolute percent errors (APEs) for model parameters across all experiments.

95% HPD intervals of average relative error from BEST analysis			
True inference model (Reference for misspecification experiments)	Median CNN APE	Median Like.-based APE	median(CNN APE - Like.-based APE)
R_0	2.4, 3.5	2.1, 3.1	0.1,1.2
δ	7.0, 10.5	5.7, 8.9	0.2, 3.0
m	9.5, 14.1	8.4, 12.1	0.4, 3.2
Misspecified R_0 experiment	Median CNN APE - median CNN Reference APE	Median Like-based APE - median Reference Like-based APE	median(CNN APE - Like-based APE)
R_0	11.8, 17.8	11.0, 16.9	-0.1, 1.6
δ	0.8, 7.6	-0.6, 5.3	1.3, 5.8
m	8.2, 17.9	6.5, 15.9	1.3, 4.7
Misspecified sample rate experiment	Median CNN APE - median CNN Reference APE	Median Like-based APE - median Reference Like-based APE	median(CNN APE - Like-based APE)
R_0	-0.3, 1.7	0.03, 1.7	0.1, 1.3
δ	12.0, 21.2	12.6, 21.4	0.1, 4.0
m	3.3, 12.0	5.6, 14.4	-1.2, 2.7
Misspecified migration rate experiment	Median CNN APE - median CNN Reference APE	Median Like-based APE - median Reference Like-based APE	median(CNN APE - Like-based APE)
R_0	-0.9, 0.8	-0.6, 1.0	-0.5, 0.8
δ	-2.3, 3.3	0.1, 5,8	-1.4, 2.3
m	4.0, 15.2	5.0, 16.2	-1.3, 2.6
Misspecified number of locations experiment	Median CNN APE - median CNN Reference APE	Median Like-based APE - median Reference Like-based APE	median(CNN APE - Like-based APE)
R_0	-0.3, 1.5	-0.7, 0.8	0.5, 1.9
δ	-0.3, 4.9	-0.5, 4.2	0.4, 3.5
m	3.4, 11.1	5.8, 13.5	-0.9, 1.6
Phylogenetic error experiment	Median CNN APE - median CNN Reference APE	Median Like-based APE - median Reference Like-based APE	median(CNN APE - Like-based APE)
R_0	0.7, 3.0	1.7, 4.4	-1.4, 0.1
δ	2.3, 9.6	1.5, 7.2	1.4, 5.3
m	-1.2, 6.0	-1.8, 5.4	-1.7, 2.4

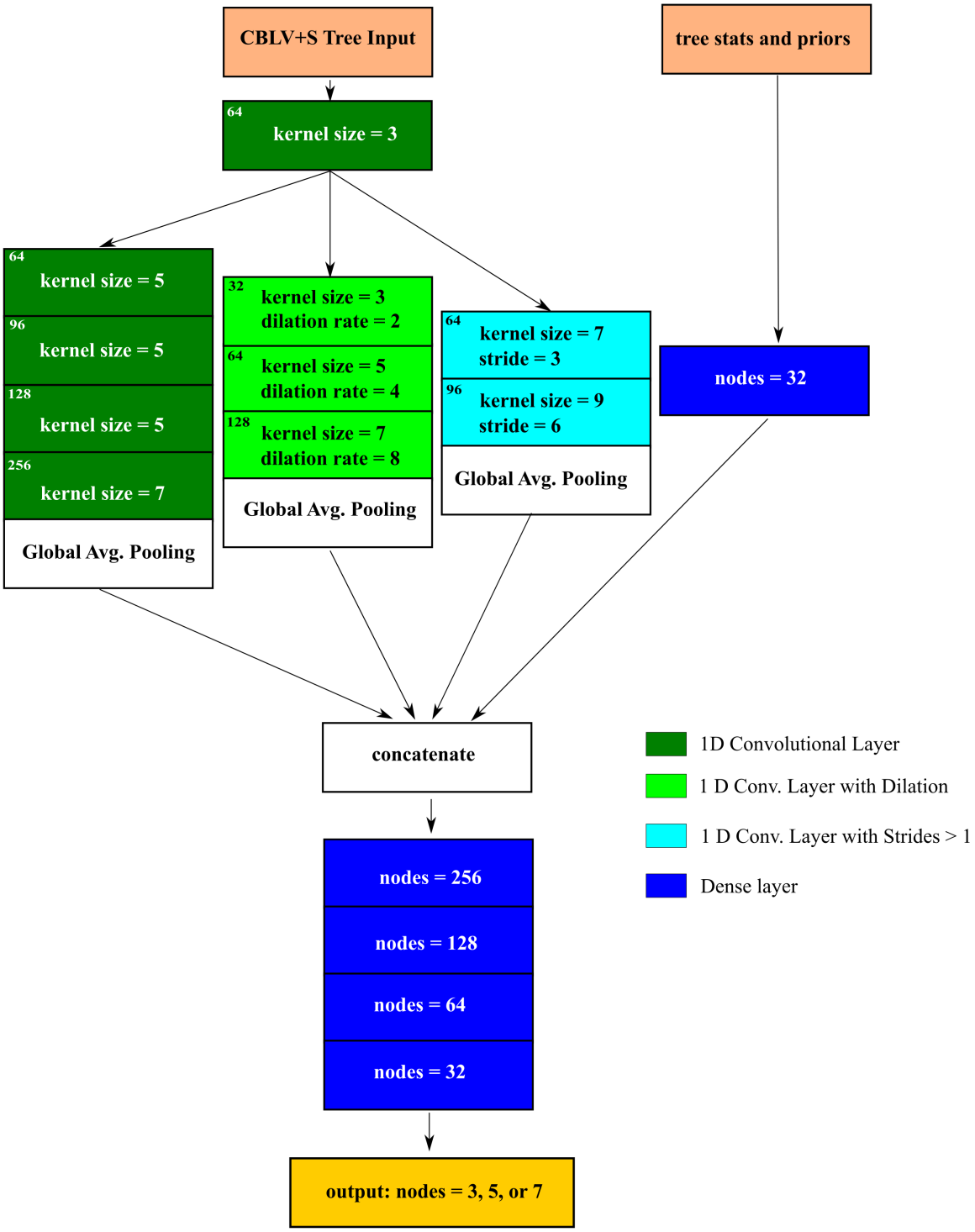

Figure S1: Diagram of deep neural network trained to make 2 kinds of predictions (rates and origin location) under two models (MTBD and SDMTBD).

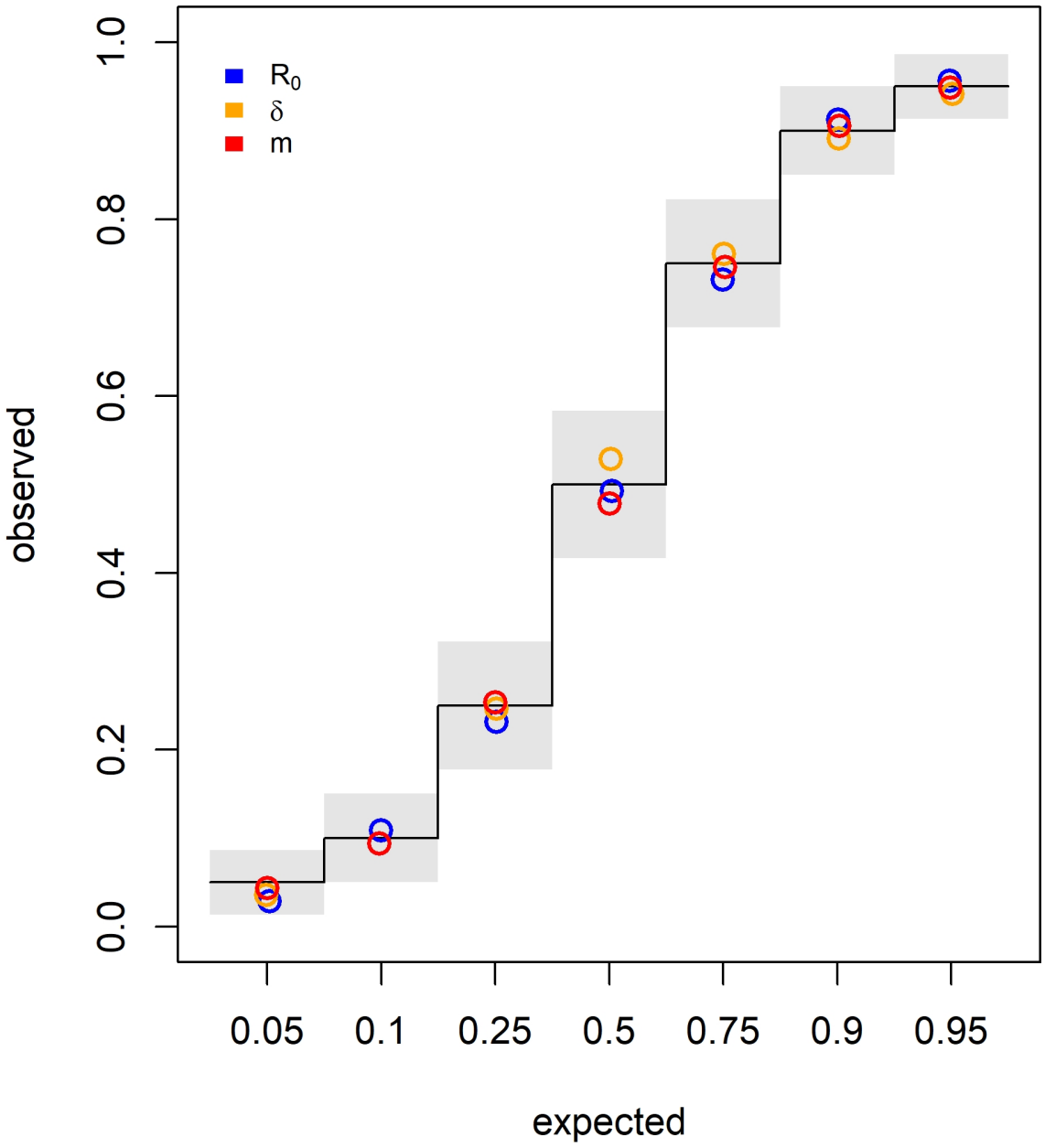

Figure S2: Coverage of posterior distributions simulated with TensorPhylo. Seven different HPD intervals were measured for coverage (labled horizontal). The expected frequency of coverage for each of the categories is shown at the black steps. Gray bands indicate the 95% confidence intervals for estimates of the binomial proportion at each of the expected values. The colored circles indicate the observed coverage of the three rate parameters at each of the expected values.

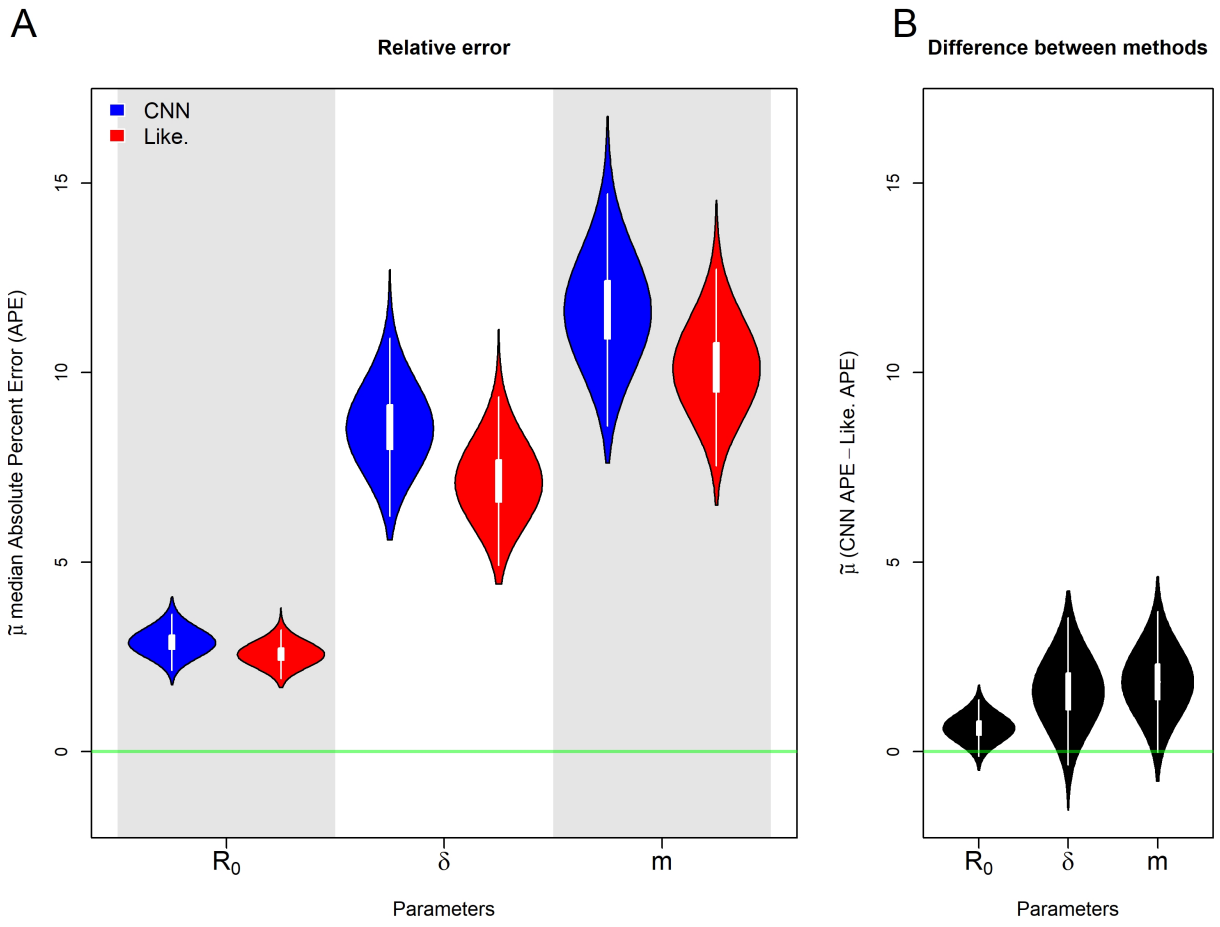

Figure S3: Posterior distributions of the population median, $\tilde{\mu}$, APE estimates of the rate parameters R_0, δ, and m under the true model. A) shows posterior distribution of the median APE for each of the 3 rate parameters estimated by the CNN (blue) and the likelihood-based method (red). The green line indicates no error. B) shows the posterior distribution for the median difference between the CNN estimate's APE and the likelihood-based estimate's APE. The green line indicates the median APE difference is zero.

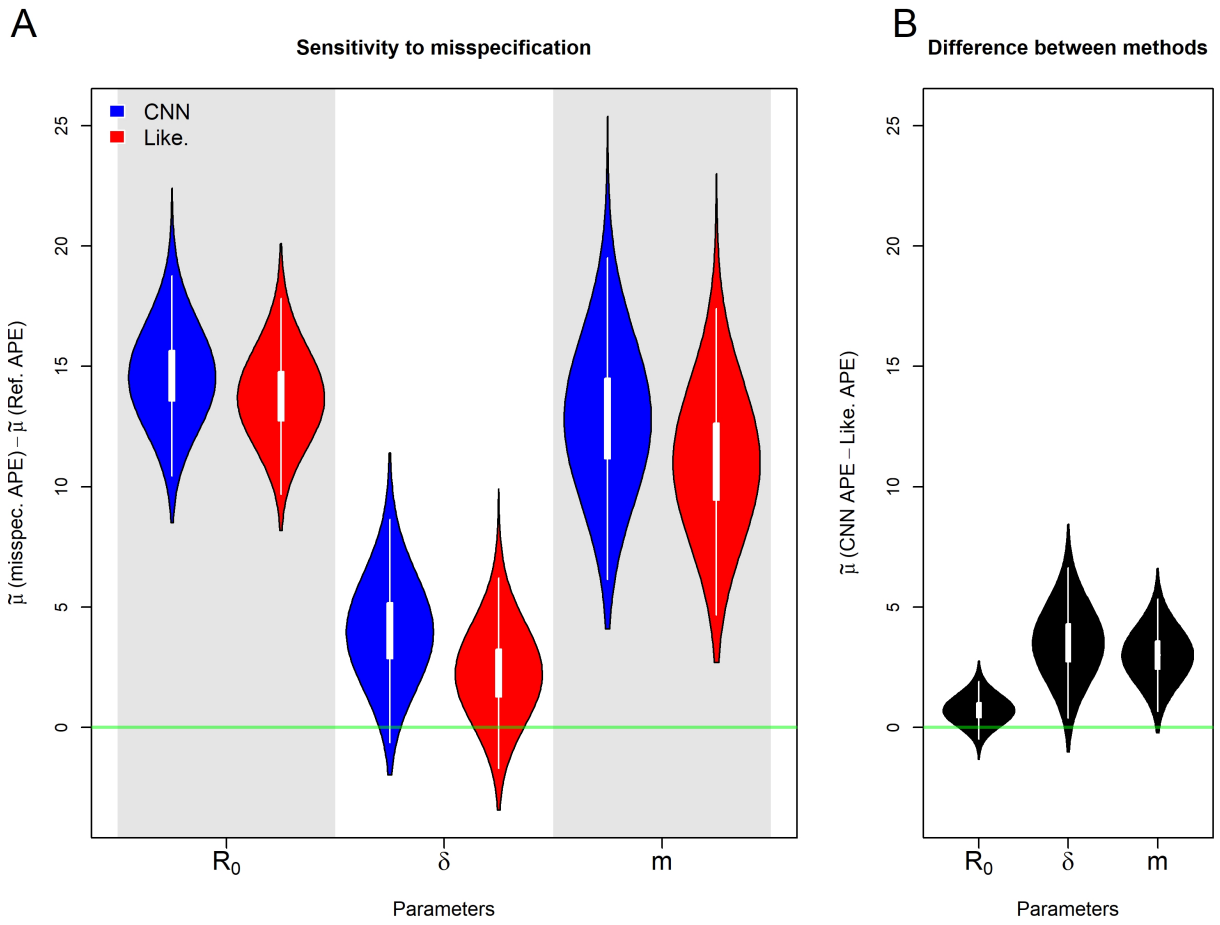

Figure S4: Posterior distributions of median, $\tilde{\mu}$, APE for the misspecified R_0 experiment. A) shows posterior distribution of the difference between the median error under the misspecified model and the the median error under the true, reference model. B) shows the posterior distribution for the population median difference between the CNN estimate's APE and the likelihood-based estimate's APE.

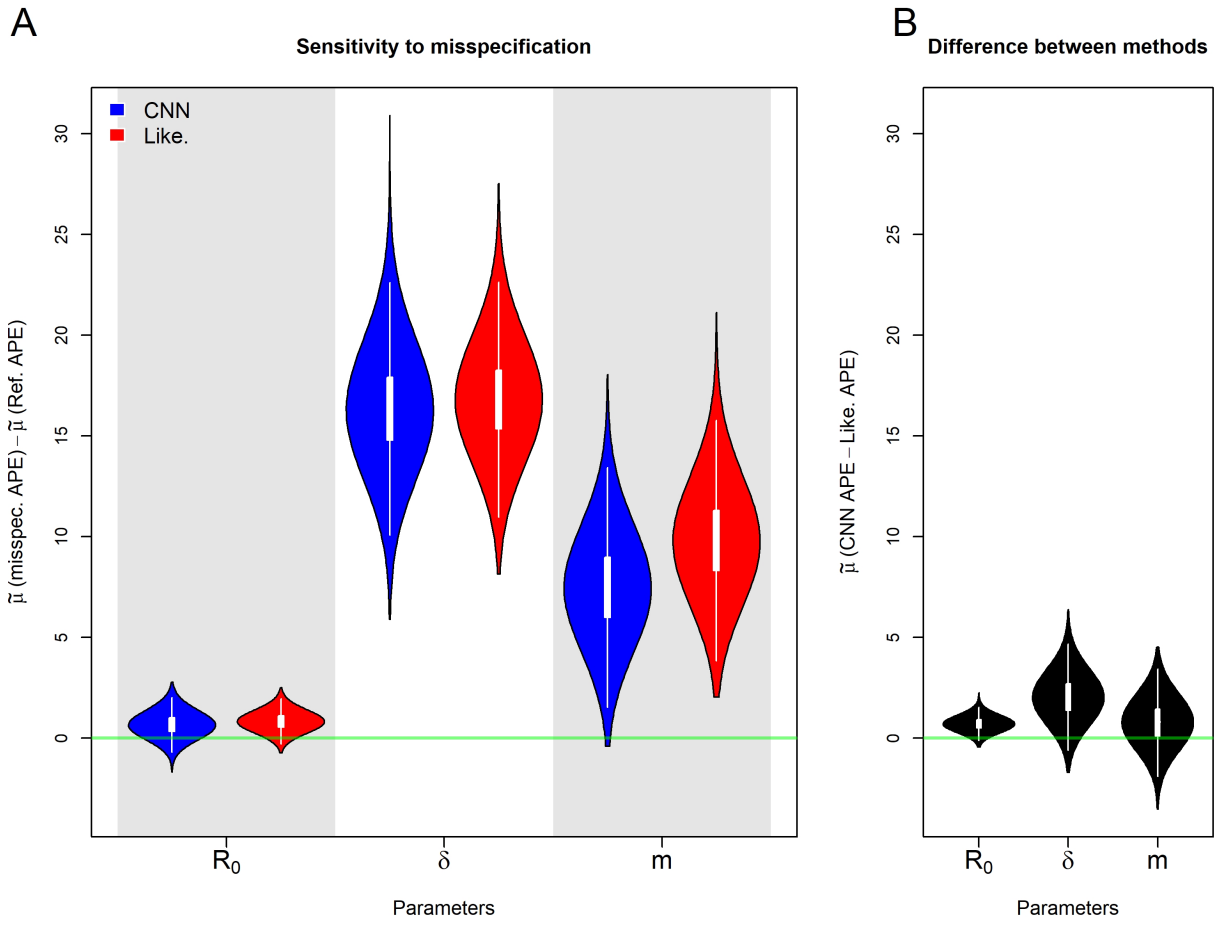

Figure S5: Posterior distributions of median, $\tilde{\mu}$, APE for the misspecified sampling rate, δ, experiment. Details are the same as in S4

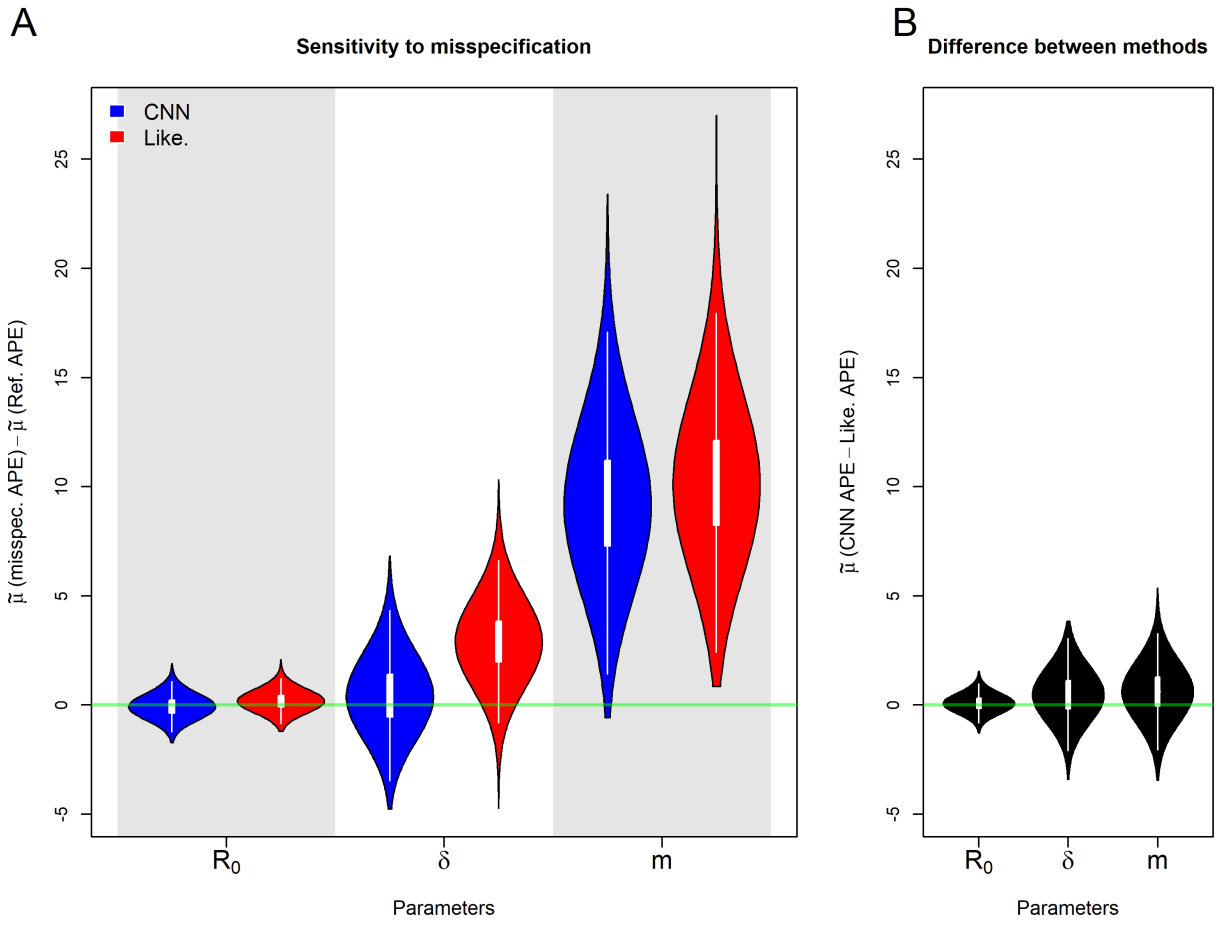

Figure S6: Posterior distributions of median, $\tilde{\mu}$, APE for the misspecified migration rate, m, experiment. Details are the same as in S4

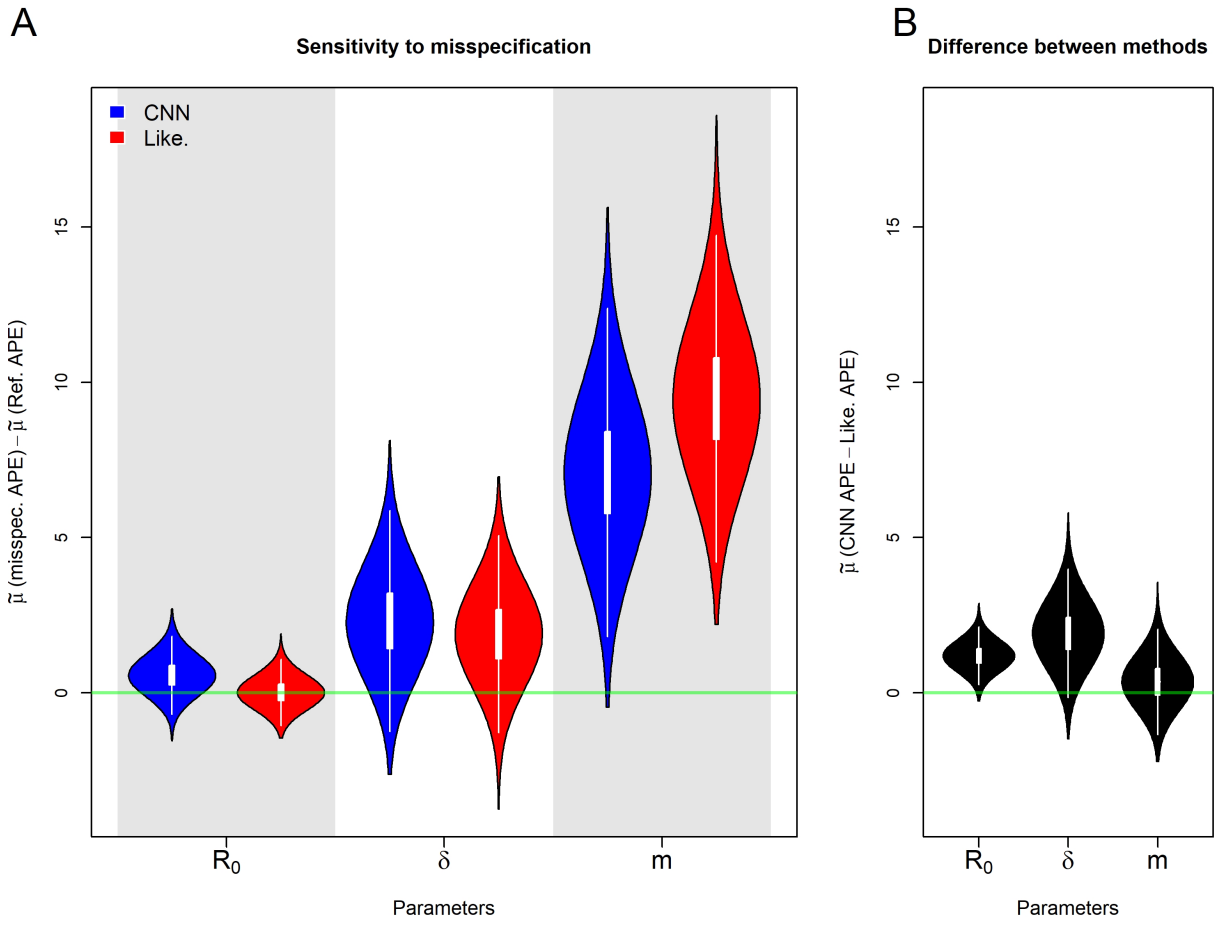

Figure S7: Posterior distributions of the median APE when the model is misspecified for the number of locations. Details are the same as in S4

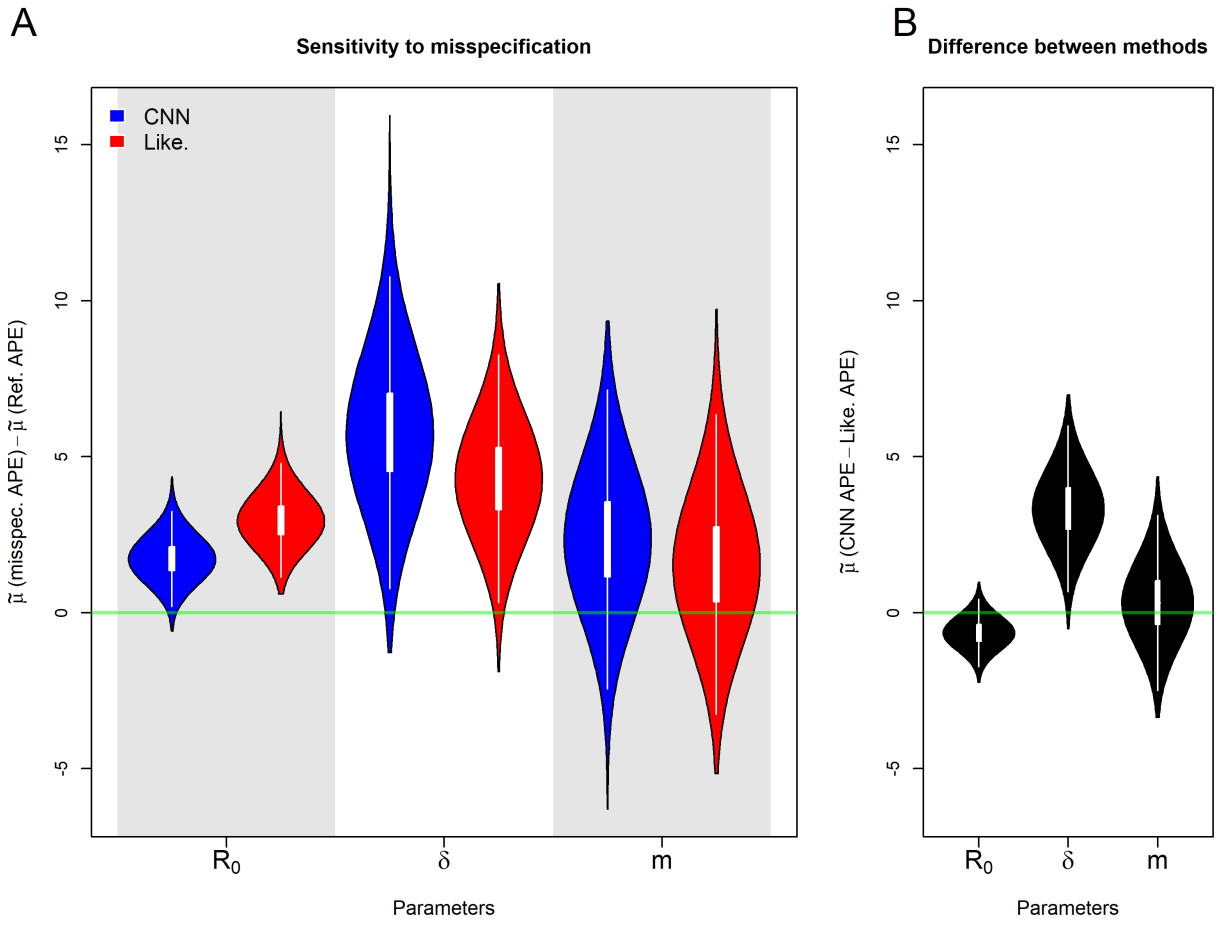

Figure S8: Posterior distributions of the median APE when the phylogenetic tree is incorrect. Details are the same as in S4